# An Elliptic Blending explicit algebraic Reynolds-stress model for wall-bounded flows

Fabien Duval, Christophe Friess

# An Elliptic Blending explicit algebraic Reynolds-stress model for wall-bounded flows

Duval, Fabien[1] and Friess, Christophe[2]

[1] Institut de Radioprotection et de Sûreté Nucléaire (IRSN), Saint Paul Lez Durance 13115, France
[2] Aix-Marseille Univ., CNRS, Centrale Marseille, M2P2 Marseille, France

**Abstract**

A new explicit algebraic Reynolds stress model is derived based on the elliptic blending strategy to account for near-wall blocking effects. The resulting model inherits some of the most important features of the underlying elliptic blending Reynolds stress model, especially the two-component limit of turbulence, but involves only one elliptic equation for the blending coefficient in addition to the standard two-equation $k$-$\varepsilon$ model which serves here as a platform for the model. The algebraic relationship is developed following a direct solution method for two- and three-dimensional mean flows rather than using a projection over a truncated integrity basis. The resulting algebraic relation remains formally similar to standard expressions based on a linear pressure-strain model with the addition of a tensor related to wall orientation. An analytical solution of the nonlinear consistency equation for the production to dissipation ratio is provided for two-dimensional cases that serves as an initial guess to an iterative approach depending on the flow situation. The computations carried out on fully developed turbulent flows to validate the algebraic model demonstrate the good model performances and confirm the effectiveness of the iterative approach to reach self consistency.

## 1 Introduction

Wall-bounded turbulent flows occur in many applications and have been the subject of intense continuous research as the near-wall region has a strong influence on the bulk flow, located far from the wall. The prediction of turbulence anisotropy and near-wall peaks may become crucial in some situations, especially in multiphysics applications. Among the situations of interest, prediction of aerosol transport and deposition in rectangular duct geometries requires a careful examination of wall-induced turbulence anisotropy that leads to secondary motions in the cross-stream plane. In this situation, while secondary motions are restricted in practice to a few percent of the streamwise bulk flow, they may have some important consequences on particle preferential concentrations [1] and then on their deposition patterns. Another situation of interest is related to air pollution in the lower part of the atmospheric boundary layer. In this layer, known as the surface layer, urban or vegetal canopy strongly interacts with the flow and the coupling between wind turbulence and near-ground induced turbulence greatly affects pollutant dispersion related for instance to carbon monoxide or particle matter emitted by industries or vehicles [2] or to radionuclides released from cyclotrons dedicated to clinical applications [3].

Early turbulence models accounted for wall vicinity by using either wall functions or damping functions. Wall functions correspond to a multi-domain approach that consists in modeling the near-wall region and applying matching conditions at a fictitious interface usually located in the logarithmic layer. The near-wall modeling is usually based on the universal law-of-the-wall theory, which is only valid in the limit of infinite Reynolds numbers, for fully-developed attached turbulent boundary layers, without adverse pressure gradients. On their part, damping functions allow the transport equations to be integrated down to the wall, and are essentially meant to imitate the effect of molecular viscosity on the shear stress, and to modulate dissipation in the vicinity of walls (see *e.g.* [4] for a review). The related damping functions are mostly empirical and do not allow to distinguish between viscous and inviscid kinematic effects that take place in the near-wall region [5]. On their part, viscous effects caused by the no-slip condition result in a damping of all components of the velocity fluctuation. On the other hand, inviscid or blocking effects caused by the impermeability condition result in a damping of velocity fluctuations that acts primarily on the wall-normal direction. Such non-viscous effects are responsible for a strongly anisotropic turbulence that tends to a two-component limit of turbulence in the vicinity of the wall.

Beside the introduction of damping functions, more rigorous approaches were proposed (*e.g.* [6, 7, 8, 9]), most of them in the frame of second-order modeling. Among the existing approaches, the *elliptic relaxation* model proposed by Durbin [7, 8] addresses specifically inviscid blocking effects, considering a two-point closure for the redistribution term of the Reynolds stress transport equation. This resulted in a $R_{ij}$-$\varepsilon$ model along with six additional transport equations for the relaxation parameters $f_{ij}$. This model was followed by numerous variants, some of which are presented hereafter. These variants include substantial simplifications without renouncing the theoretical background of the original version and further include extensions to scalar turbulent fluxes. These are the main motivations that lead here to focus on this family of models.

As a first simplification of elliptic relaxation, Durbin derived an eddy-viscosity model inspired of elliptic relaxation, namely $\overline{v^2}$-$f$. It consists in a four equation model for $k$, $\varepsilon$, the wall-normal turbulent stress and the relaxation parameter. Similar eddy-viscosity variants were proposed for instance by Hanjalić *et al.* [10] and Billard and Laurence [11]. These approaches share the feature of solving four equations for turbulence quantities. In the framework of full Reynolds stress models, Manceau and Hanjalić proposed the *elliptic blending* model [12, 5, 13]. The difference with elliptic relaxation lies in the fact that the elliptic blending model solves, besides momentum, Reynolds stresses and dissipation, one single additional differential equation for a blending parameter $\alpha$, instead of the six $f_{ij}$'s. Attempts have then been made to reduce further the complexity of the model by deriving a $k$-$\varepsilon$-$\alpha$ model, in the fashion of explicit algebraic models. Such approaches consist roughly in replacing the linear Boussinesq relationship involved in the eddy-viscosity model (usually called *platform* model) by a more general nonlinear stress relationship, the latter being inspired from an equilibrium assumption in the Reynolds stresses transport equation. The resulting model thus inherits simplicity from the eddy-viscosity model, and more complex physics from the Reynolds-stress closure. Among numerous explicit algebraic models, the first involving the elliptic blending strategy [14, 15] was based on a projection on a three-term tensorial basis. It proved successful in the prediction of two-dimensional flows, reproducing proper near-wall turbulence features, especially the two-component limit. Interestingly, this $k$-$\varepsilon$-$\alpha$ performed at least as well as $\overline{v^2}$-$f$, while resolving one less equation.

In the present paper, a novel explicit algebraic Reynolds-stress model, based on the elliptic blending strategy, is derived in Sec. 2 for two- and three-dimensional mean flows. The algebraic relation is obtained here following a direct solution method rather than using a truncating three-term tensorial basis. A methodology is provided to obtain a self-consistent model on the basis of an analytical solution of the production to dissipation ratio for two-dimensional mean flows parallel

to the wall. The platform model based on the two-equation $k$-$\varepsilon$ model is presented in Sec. 3. The new explicit algebraic model is then tested in Sec. 4 first a priori with respect to DNS data of fully turbulent channel flow, and then upon several test cases: channel with and without ribs, square duct. Then, some conclusions are drawn and some future prospects are presented in Sec. 5.

## 2 Explicit algebraic Reynolds-stress models

For constant density flows, the Reynolds-averaged transport equations governing the flow read

$$\frac{\partial \overline{u}_i}{\partial x_i} = 0 \tag{1}$$

$$\frac{\partial \overline{u}_i}{\partial t} + \overline{u}_j \frac{\partial \overline{u}_i}{\partial x_j} = -\frac{1}{\rho}\frac{\partial \overline{p}}{\partial x_i} + \frac{\partial}{\partial x_j}\left(\nu \frac{\partial \overline{u}_i}{\partial x_j} - \overline{u'_i u'_j}\right) \tag{2}$$

where $u_i$ is the velocity, $\rho$ the density, $p$ the pressure and $\nu$ the kinematic viscosity. The overbar denotes a statistical-averaged quantity while $u'_i = u_i - \overline{u}_i$ corresponds to the velocity turbulent fluctuations. The turbulent fluxes $\overline{u'_i u'_j}$ which appear in the averaged transport equations Eqs. 2, refer to the Reynolds stresses that remain to be modeled to obtain a closed turbulence model.

To that aim, additional transport equations can be derived and these form the basis of second order or differential Reynolds-stress models. These equations are obtained by multiplying the equations for the turbulent fluctuations $u'_i$ by $u'_j$, adding the corresponding equations obtained by switching subscripts $i$ and $j$ and then averaging the result. The obtained transport equations read

$$\frac{\partial \overline{u'_i u'_j}}{\partial t} + \overline{u}_k \frac{\partial \overline{u'_i u'_j}}{\partial x_k} - \mathcal{D}_{ij} = \mathcal{P}_{ij} + \Pi_{ij} - \varepsilon_{ij} \tag{3}$$

where $\mathcal{D}_{ij}$, $\mathcal{P}_{ij}$, $\Pi_{ij}$ and $\varepsilon_{ij}$ refer respectively to diffusion, production, pressure redistribution and dissipation of the Reynolds stresses. The production term requires no model and reads

$$\mathcal{P}_{ij} = -\overline{u'_i u'_k}\frac{\partial \overline{u}_j}{\partial x_k} - \overline{u'_j u'_k}\frac{\partial \overline{u}_i}{\partial x_k} \tag{4}$$

On the other hand, models are required for the dissipation rate and the pressure redistribution terms and remain to be specified. In regions far from the wall, the dissipation rate tensor is usually assumed to be isotropic and thus reads

$$\varepsilon_{ij} = \frac{2}{3}\varepsilon\delta_{ij} \tag{5}$$

Far from the wall, the pressure redistribution term can be expressed following the model proposed by Rotta [16] for the slow pressure strain and the LRR model proposed by Launder, Reece and Rodi [17] for the rapid part

$$\begin{aligned}\Pi_{ij} = &- c_1 \frac{\varepsilon}{k}\left(\overline{u'_i u'_j} - \frac{2}{3}k\delta_{ij}\right) - \frac{c_2+8}{11}\left(\mathcal{P}_{ij} - \frac{1}{3}\mathcal{P}_{kk}\delta_{ij}\right) \\ &- \frac{30c_2-2}{55}k\left(\frac{\partial \overline{u}_i}{\partial x_j} + \frac{\partial \overline{u}_j}{\partial x_i}\right) - \frac{8c_2-2}{11}\left(-\overline{u'_i u'_k}\frac{\partial \overline{u}_k}{\partial x_j} - \overline{u'_j u'_k}\frac{\partial \overline{u}_k}{\partial x_i} - \frac{1}{3}\mathcal{P}_{kk}\right)\end{aligned} \tag{6}$$

where $c_1$ and $c_2$ are constants that remain to be specified. In the above relations, $k = \overline{u'_i u'_i}/2$ and $\varepsilon$ refer respectively to the turbulent kinetic energy and its dissipation rate for which transport equations remain to be given. This constitutes the so-called platform model, which will be discussed in Sec. 3.

As outlined in [18], Eq. 6 is the most general linear form for the pressure-redistribution term. While linear pressure-strain models are particularly well suited in developing explicit algebraic Reynolds stress models, quasi-linear models complicate the developments but may provide a more accurate modeling in some situations. As usual, quasi-linear models refer to pressure-strain models that remain tensorially linear in the dimensionless anisotropy tensor $a_{ij}$ defined by

$$a_{ij} = \frac{\overline{u_i' u_j'}}{k} - \frac{2}{3}\delta_{ij} \tag{7}$$

Inserting $a_{ij}$ in the linear pressure-strain model reads

$$\begin{aligned}\frac{\Pi_{ij}}{\varepsilon} = &-c_1 a_{ij} + \frac{4}{5}S_{ij} + \frac{9c_2+6}{11}\left(a_{ik}S_{kj} + S_{ik}a_{kj} - \frac{2}{3}a_{kl}S_{lk}\delta_{ij}\right) \\ &+ \frac{7c_2-10}{11}\left(a_{ik}\Omega_{kj} - \Omega_{ik}a_{kj}\right)\end{aligned} \tag{8}$$

where $S_{ij}$ and $\Omega_{ij}$ denote the normalized mean strain tensor and the normalized mean rotation tensor respectively given as

$$S_{ij} = \frac{\tau}{2}\left(\frac{\partial \overline{u}_i}{\partial x_j} + \frac{\partial \overline{u}_j}{\partial x_i}\right), \quad \Omega_{ij} = \frac{\tau}{2}\left(\frac{\partial \overline{u}_i}{\partial x_j} - \frac{\partial \overline{u}_j}{\partial x_i}\right) \tag{9}$$

The turbulent time scale used to normalize the velocity gradients is expressed following the limitation procedure proposed by Durbin [7] that introduces a lower bound active in the near-wall region where the turbulent time scale goes to zero:

$$\tau = \max\left(\frac{k}{\varepsilon}, C_\tau\sqrt{\frac{\nu}{\varepsilon}}\right) \tag{10}$$

The lower bound corresponds to the Kolmogorov scale for which the usual value $C_\tau = 6$ is adopted. Moving to quasi-linear models, the most representative model corresponds to the following expression that results from a linearization of the Speziale *et al.* [19] SSG model

$$\begin{aligned}\frac{\Pi_{ij}}{\varepsilon} = &-\left(b_1 - b_1^* II_{aS}\right)a_{ij} + b_2\left(a_{ik}a_{kj} - \frac{1}{3}II_a\delta_{ij}\right) + \left(b_3 - b_3^*\sqrt{II_a}\right)S_{ij} \\ &+ b_4\left(a_{ik}S_{kj} + S_{ik}a_{kj} - \frac{2}{3}II_{aS}\delta_{ij}\right) - b_5\left(a_{ik}\Omega_{kj} - \Omega_{ik}a_{kj}\right)\end{aligned} \tag{11}$$

where we have adopted the notations

$$II_{aS} = a_{kl}S_{lk}, \quad II_a = a_{kl}a_{lk} \tag{12}$$

The $b_2$-term, which is tensorially nonlinear in $a_{ij}$, is usually removed to improve numerical robustness [13] so that the above quasi-linear expression with $b_2 = 0$ remains quite general. In the frame of explicit algebraic Reynolds stress models, it is of great interest to reduce the nonlinearity of the pressure-strain model in order to simplify the algebraic relation and to obtain a fully consistent model for which the production to dissipation ratio results in the solution of the algebraic relation. As a result, the use of non-zero values for $b_1^*$ and $b_3^*$ that refer to the SSG model in Table. 1 usually requires a fixed value for $II_{aS}$ or $II_a$ to obtain a fully explicit algebraic model. Some of the drawbacks linked to these approximations are discussed in details in [18] and this motivates the use of a fully linear pressure-strain model. The fully linear pressure-strain model as proposed by Wallin & Johansson [18] is adopted here. Following the linearized SSG model proposed in [14] which is obtained by neglecting the quadratic anisotropy term and approximating the $II_a$ invariant by $\sqrt{1-f}$, a correction that refers to a SSG-like model is also assessed by using $b_3^* = b_3$.

| | $b_1$ | $b_1^*$ | $b_3$ | $b_3^*$ | $b_4$ | $b_5$ |
|---|---|---|---|---|---|---|
| LRR [17] | 1.5 | 0 | 0.8 | 0 | 0.87 | 0.65 |
| Wallin & Johansson [18] | 1.8 | 0 | 0.8 | 0 | 1 | 0.55 |
| SSG [19] ($b_2 = 0$) | 1.7 | 0.9 | 0.8 | 0.65 | 0.62 | 0.2 |

Table 1: Coefficients for some of quasi-linear pressure-strain models

### 2.1 Elliptic blending

In the near-wall region, the dissipation and the pressure redistribution terms take different expressions as provided by Eqs. 5 and 11. Following the elliptic blending approach, the difference between pressure redistribution and dissipation is expressed as:

$$\Pi_{ij} - \varepsilon_{ij} = (1-f)\left(\Pi_{ij}^w - \varepsilon_{ij}^w\right) + f\left(\Pi_{ij}^h - \varepsilon_{ij}^h\right) \tag{13}$$

where superscripts $h$ and $w$ refer respectively to the homogeneous and near-wall modeling. The blending function $f$ which takes values between zero at the wall and one far from the wall is determined from $f = \alpha^p$ where $\alpha$ refers to the elliptic coefficient which is solution of the following elliptic equation supplemented by the boundary condition $\alpha = 0$ at the wall:

$$\alpha - L^2\nabla^2\alpha = 1 \tag{14}$$

where $L$ is the turbulent length scale given by [7]:

$$L = C_L \max\left(\frac{k^{3/2}}{\varepsilon}, C_\eta\eta\right) \tag{15}$$

Values of the constants entering the above equation, are given in Tab 3. The blending function $f$ entering Eq. 13 or, in an equivalent way, the exponent $p$ involved in $f = \alpha^p$, is calibrated from Eq. 13 for the wall-normal direction, denoted here using the subscript 2, as follows:

$$f = \frac{(\Pi_{22} - \varepsilon_{22}) - (\Pi_{22}^w - \varepsilon_{22}^w)}{(\Pi_{22}^h - \varepsilon_{22}^h) - (\Pi_{22}^w - \varepsilon_{22}^w)} \tag{16}$$

It can be shown that the proper asymptotic behaviours are respected with $f = \alpha^3$ but, in practice, the choice $f = \alpha^2$ leads to very similar results [13].

While the homogeneous modeling of dissipation and pressure distribution has been briefly reviewed in the previous section and are given respectively by Eqs. 5 and 11, it remains to deal with the near-wall modeling. Adopting Rotta's model, the near-wall modeling of the dissipation tensor reads:

$$\varepsilon_{ij}^w = \frac{\overline{u_i'u_j'}}{k}\varepsilon \tag{17}$$

On the other hand, according to Manceau [13], the near-wall modeling of the pressure redistribution tensor that replicates the same wall-limiting values as the elliptic relaxation approach can be expressed as:

$$\Pi_{ij}^w = -\varepsilon\left(a_1 a_{ij} + a_2\left(1 + a_2' II_{aM}\right)M_{ij} + a_3\left(a_{ik}M_{jk} + a_{jk}M_{ik} - \frac{2}{3}II_{aM}\delta_{ij}\right)\right) \tag{18}$$

where $a_1$, $a_2$, $a_2'$ and $a_3$ are constants, $II_{aM} = a_{lk}M_{kl}$ and $M_{ij}$ refers to the deviatoric part of $n_i n_j$ defined by

$$M_{ij} = n_i n_j - \frac{1}{3}\delta_{ij} \tag{19}$$

where $\boldsymbol{n}$ is the wall-normal normalized vector, pointing inside the fluid domain. The expression (18) for the pressure redistribution tensor is symmetric and remains traceless. The constants can be determined from the near-wall equilibrium relationship deduced from the Reynolds stress budget:

$$\Pi_{ij}^w - \varepsilon_{ij}^w = -\nu \frac{\partial^2 \overline{u_i' u_j'}}{\partial y^2} \tag{20}$$

where $y$ refers here to the coordinate normal to the wall. Introducing the asymptotic behavior of the right hand side leads to:

$$\Pi_{ij}^w - \varepsilon_{ij}^w = -n(n+1) \lim_{y\to 0} \nu \frac{\overline{u_i' u_j'}}{y^2} \tag{21}$$

where $n = 1$ for $\overline{u'^2}$, $\overline{w'^2}$ and $\overline{u'w'}$; $n = 2$ for $\overline{u'v'}$ and $\overline{v'w'}$; and $n = 3$ for $\overline{v'^2}$. The solution of the resulting second order differential equation for $\overline{u_i' u_j'}$ together with boundary conditions $\overline{u_i' u_j'} = 0$ leads formally at the leading order to $\overline{u_i' u_j'} = r_{ij} y^{n+1}$. Assuming that $y$ corresponds to the wall-normal direction, the asymptotic behaviour of the near-wall pressure-strain rate has been assumed to have the following form:

$$\Pi_{ij}^w = -\frac{\varepsilon}{k} \begin{pmatrix} -\frac{d}{2}\overline{v'^2} & c\overline{u'v'} & 0 \\ c\overline{u'v'} & d\overline{v'^2} & c\overline{v'w'} \\ 0 & c\overline{v'w'} & -\frac{d}{2}\overline{v'^2} \end{pmatrix} \tag{22}$$

Hence, this results in the following relations that allow the determination of the constants $a_1$, $a_2$, $a_2'$ and $a_3$ from $d$ and $c$:

$$a_1 = \frac{2c}{3}, \quad a_2 = d, \quad a_2' = \frac{3d - 4c}{2d}, \quad a_3 = c \tag{23}$$

The theoretical asymptotic behaviour corresponds to $c = 2$ and $d = 5$, leading to $a_1 = 4/3$, $a_2 = 5$, $a_2' = 7/10$, whereas the asymptotic behaviour related to the Durbin's elliptic relaxation Reynolds-stress model [8] corresponds to $c = d = 5$ and this leads to $a_1 = 10/3$, $a_2 = 5$, $a_2' = -1/2$ and $a_3 = 5$. As observed by Manceau and Hanjalić [5], the use of the coefficients corresponding to the exact asymptotic behaviour surprisingly worsens the results of the elliptic blending Reynolds stress model in a channel flow. This unexpected result was later discussed by Manceau [13] and comes from the buffer layer where the blending with $\Pi_{ij}^h$ part leads to a significant underestimation of $\Pi_{ij}$ using the asymptotically exact formulation contrary to Durbin's empirical formulation. Here, an alternate empirical formulation is proposed by keeping $d = 5$ for $\Pi_{11}^w$, $\Pi_{22}^w$ and $\Pi_{33}^w$ but prescribing $c = 15/4$ for $\Pi_{12}^w$ and $\Pi_{23}^w$. This intermediate value for $c$ remains close to the original empirical value but allows to substantially reduce the complexity of the development of an explicit algebraic model as this leads to $a_2' = 0$ and thus, this reduces in Eq. 18 the non-linearity with respect to $M_{ij}$.

## 2.2 Weak equilibrium assumption and algebraic model

Algebraic models are based on the weak-equilibrium assumption that states that the advection and diffusion of the dimensionless Reynolds-stress anisotropy tensor can be neglected. The first step

consists thus in writing the transport equations for the Reynolds stresses in terms of the dimensionless anisotropy tensor:

$$\frac{da_{ij}}{dt} = \frac{1}{k}\frac{d\overline{u_i'u_j'}}{dt} - \frac{\overline{u_i'u_j'}}{k}\frac{dk}{dt} \tag{24}$$

The transport equation for the turbulent kinetic energy is obtained by taking half the trace of Eq. 3 and can be written as

$$\frac{dk}{dt} - \mathcal{D} = \mathcal{P} - \varepsilon \tag{25}$$

where the production is given by

$$\mathcal{P} = \frac{1}{2}\mathcal{P}_{ii} = -\overline{u_i'u_j'}\frac{\partial \overline{u}_i}{\partial x_j} \tag{26}$$

Then, from Eqs. 3, 25 and 24, the previous equation can be written as

$$\frac{da_{ij}}{dt} - \frac{1}{k}\left(\mathcal{D}_{ij} - \frac{\overline{u_i'u_j'}}{k}\mathcal{D}\right) = \frac{1}{k}\left(\mathcal{P}_{ij} + \Pi_{ij} - \varepsilon_{ij} - \frac{\overline{u_i'u_j'}}{k}\left(\mathcal{P} - \varepsilon\right)\right) \tag{27}$$

Using the weak-equilibrium assumption, the left-hand side of the previous equation is removed and the resulting algebraic equations read

$$\frac{\overline{u_i'u_j'}}{k}\left(\mathcal{P} - \varepsilon\right) = \mathcal{P}_{ij} + \Pi_{ij} - \varepsilon_{ij} \tag{28}$$

The above class of models is termed as algebraic stress models as it only requires the solution of an implicit algebraic equation for the Reynolds stresses. The production and pressure-strain terms on the right hand side of the above equation can be expressed in terms of $a_{ij}$, $S_{ij}$ and $\Omega_{ij}$. Inserting $a_{ij}$, $S_{ij}$ and $\Omega_{ij}$ in the definition of the production and the near-wall dissipation terms leads to the following expressions

$$\frac{\mathcal{P}_{ij}}{\varepsilon} = -\frac{4}{3}S_{ij} - \left(a_{ik}S_{kj} + S_{ik}a_{kj}\right) + a_{ik}\Omega_{kj} - \Omega_{ik}a_{kj} \tag{29}$$

$$\frac{\varepsilon_{ij}^w}{\varepsilon} = a_{ij} + \frac{2}{3}\delta_{ij} \tag{30}$$

As a result, the algebraic equation for the Reynolds stress anisotropy tensor, accounting for elliptic blending, reads

$$\begin{aligned}\left(\frac{\mathcal{P}}{\varepsilon}\left(1 + b_1^* f\right) + f b_1 - 1 + (1-f)(a_1+1)\right) a_{ij} = &-\left(\frac{4}{3} - \left(b_3 - b_3^*\sqrt{II_a}\right) f\right) S_{ij} \\ &- (1-f)\, a_2 \left(1 + a_2' II_{aM}\right) M_{ij} + (1 - b_5 f)\left(a_{ik}\Omega_{kj} - \Omega_{ik}a_{kj}\right) \\ &- (1 - b_4 f)\left(a_{ik}S_{kj} + S_{ik}a_{kj} - \frac{2}{3}II_{aS}\delta_{ij}\right) \\ &- (1-f)\, a_3 \left(a_{ik}M_{jk} + a_{jk}M_{ik} - \frac{2}{3}II_{aM}\delta_{ij}\right)\end{aligned} \tag{31}$$

As outlined by Wallin and Johansson [18], in the frame of the LRR model, the value of $c_2$ close to 5/9 suggested by some studies leads to $b_4 = 1$ and this greatly simplifies the algebraic equation

without elliptic blending, namely substituting $f = 1$ in Eq. 31, as this allows to remove the fourth term in the right hand side. Adopting this value in the frame of elliptic blending allows to write the algebraic relation in a more compact form as:

$$\begin{aligned} N a_{ij} = &-C_1 \tilde{S}_{ij} - \beta_m M_{ij} + (a_{ik}\Omega_{kj} - \Omega_{ik}a_{kj}) \\ &- C_2 \left( a_{ik}\tilde{S}_{kj} + \tilde{S}_{ik}a_{kj} - \frac{2}{3} II_{a\tilde{S}} \delta_{ij} \right) \end{aligned} \tag{32}$$

where we have introduced the following notations:

$$\tilde{S}_{ij} = S_{ij} + a_3 M_{ij} \tag{33}$$

$$\beta_m = a_2 C_2 \left(1 + a_2' II_{aM}\right) - a_3 C_1 \tag{34}$$

$$II_{a\tilde{S}} = a_{lk}\tilde{S}_{kl} = II_{aS} + a_3 II_{aM} \tag{35}$$

The coefficients $C_1$, $C_2$ and $N$ are given by:

$$C_1 = C_3 \left( \frac{4}{3} - \left( b_3 - b_3^* \sqrt{II_a} \right) f \right), \quad C_2 = (1-f)C_3, \quad N = c_1' + C_3 \left(1 + b_1^* f\right) \frac{\mathcal{P}}{\varepsilon} \tag{36}$$

with:

$$C_3 = \frac{9}{9 - 5f}, \quad c_1' = C_3 \left( f c_1 - 1 + (1-f)(a_1 + 1) \right) \tag{37}$$

It should be pointed out that the above relations for the model coefficients are modified according to the diffusion correction proposed by Wallin and Johansson [18] to deal with regions of the flow where the production to dissipation ratio is small and where the weak equilibrium assumption is expected to fail. The correction consists here in modifying the coefficient $c_1'$ according to

$$c_1' = C_3 \left( f \left( c_1 + f C_{\mathrm{D}} \max \left( 1 - \frac{\mathcal{P}}{\varepsilon}, 0 \right) \right) - 1 + (1-f)(a_1 + 1) \right) \tag{38}$$

Here the correction uses the standard coefficient value $C_{\mathrm{D}} = 2.2$ [18] times the blending function $f$ in order to remove the correction in the vicinity of the wall where the production to dissipation ratio is small.

In this work, rather than truncating a priori the integrity basis as proposed in [14, 15], a direct solution of Eq. 32 for $a_{ij}$ is proposed following the methodology outlined by Grigoriev and Lazeroms [20]. The direct solution method is described in the following sections, in Sec. 2.3 for two-dimensional mean flows and in Sec. 2.4 for three-dimensional mean flows. An efficient strategy is then proposed in Sec. 2.5 to obtain a self-consistent model.

### 2.3 Explicit algebraic model for two-dimensional mean flows

For two-dimensional mean flows, $a_{i3} = a_{3i} = 0$ for $i = 1, 2$ but $a_{33}$ may be non-zero. In the same way, $M_{i3} = M_{3i} = 0$ but $M_{33} = -1/3 \neq 0$. Hence, we first define the two-dimensional traceless analog of $a_{ij}$ and $M_{ij}$ by:

$$a_{ij} = a_{ij}^{(2D)} + \beta_{w0} \left( \delta_{ij}^{(2D)} - \frac{2}{3}\delta_{ij} \right) \tag{39}$$

$$M_{ij} = M_{ij}^{(2D)} + \frac{1}{2} \left( \delta_{ij}^{(2D)} - \frac{2}{3}\delta_{ij} \right) \tag{40}$$

where $\beta_{w0}$ is a coefficient that accounts for a non-zero $a_{33}$ component and that remains to be determined. In order to obtain an algebraic relation for $a_{ij}^{(2D)}$, we first write the following identities:

$$a_{ik}S_{jk} = a_{ik}^{(2D)}S_{jk} + \frac{\beta_{w0}}{3}S_{ij} \tag{41}$$

$$a_{ik}M_{jk} = a_{ik}^{(2D)}M_{jk}^{(2D)} + \frac{1}{6}a_{ij}^{(2D)} + \frac{\beta_{w0}}{3}M_{ij}^{(2D)} - \frac{\beta_{w0}}{3}\left(\frac{1}{2}\delta_{ij}^{(2D)} - \frac{2}{3}\delta_{ij}\right) \tag{42}$$

As a result, we get:

$$II_{aS} = a_{mk}S_{km} = a_{mk}^{(2D)}S_{km} = II_{aS^{(2D)}} \tag{43}$$

$$II_{aM} = a_{mk}M_{km} = a_{mk}^{(2D)}M_{km}^{(2D)} = II_{aM^{(2D)}} + \frac{\beta_{w0}}{3} \tag{44}$$

As the strain and vorticity tensors can be treated as two-dimensional, *i.e* $S_{3i} = 0$ and $\Omega_{3i} = 0$, their two-dimensional analogs remain the same and using the above relations the algebraic equation can be written as an equation for $a_{ij}^{(2D)}$ and $\beta_{w0}$ as:

$$\begin{aligned}
&a_{ij}^{(2D)}\left(N + C_2\frac{a_3}{3}\right) + \beta_{w0}N\left(\delta_{ij}^{(2D)} - \frac{2}{3}\delta_{ij}\right) \\
&= -\left(C_1 + \frac{2\beta_{w0}}{3}C_2\right)\tilde{S}_{ij}^{(2D)} - \beta_m M_{ij}^{(2D)} + \left(a_{ik}^{(2D)}\Omega_{kj} - \Omega_{ik}a_{kj}^{(2D)}\right) \\
&- C_2\left(a_{ik}^{(2D)}\tilde{S}_{kj}^{(2D)} + \tilde{S}_{ik}^{(2D)}a_{kj}^{(2D)} - II_{a\tilde{S}^{(2D)}}\delta_{ij}^{(2D)}\right) \\
&+ C_2\left(-\frac{a_2}{2}\left(1 + a_2' II_{aM}\right) - II_{a\tilde{S}^{(2D)}} + \frac{\beta_{w0}}{3}a_3\right)\left(\delta_{ij}^{(2D)} - \frac{2}{3}\delta_{ij}\right)
\end{aligned} \tag{45}$$

where the following notations are adopted:

$$\tilde{S}_{ij}^{(2D)} = S_{ij} + a_3 M_{ij}^{(2D)} \tag{46}$$

$$II_{a\tilde{S}^{(2D)}} = a_{mk}^{(2D)}\tilde{S}_{km}^{(2D)} = II_{a\tilde{S}} - \frac{\beta_{w0}}{3}a_3 \tag{47}$$

The coefficient $\beta_{w0}$ is determined by equating the three-dimensional tensor groups on both sides of Eq. 45

$$\beta_{w0}N = C_2\left(-\frac{a_2}{2} - II_{aS} - II_{aM^{(2D)}}\left(\frac{a_2 a_2'}{2} + a_3\right) - \frac{\beta_{w0}}{3}\left(\frac{a_2 a_2'}{2} - a_3\right)\right) \tag{48}$$

The remaining part is purely two-dimensional and reads:

$$\begin{aligned}
Na_{ij}^{(2D)} = &-\left(C_1 + \frac{2}{3}\beta_{w0}C_2\right)\tilde{S}_{ij}^{(2D)} - \beta_m M_{ij}^{(2D)} + \left(a_{ik}^{(2D)}\Omega_{kj} - \Omega_{ik}a_{kj}^{(2D)}\right) \\
&- C_2\left(a_{ik}^{(2D)}\tilde{S}_{kj}^{(2D)} + \tilde{S}_{ik}^{(2D)}a_{kj}^{(2D)} - II_{a\tilde{S}^{(2D)}}\delta_{ij}^{(2D)}\right)
\end{aligned} \tag{49}$$

The expression for $N$ remains formally unchanged except that $c_1'$ is now given by:

$$c_1' = C_3\left(fc_1 - 1 + (1-f)\left(a_1 + 1 + \frac{a_3}{3}\right)\right) \tag{50}$$

Using the above relation together with the particular value $a_2' = 0$, the relation for $\beta_{w0}$ now reads:

$$\beta_{w0}\left(N - \frac{2}{3}a_3 C_2\right) = -C_2\left(II_{a\tilde{S}^{(2D)}} + \frac{a_2}{2}\right) \tag{51}$$

Hence, introducing $\tilde{s}_{ij} \equiv (C_1 + 2\beta_{w0}C_2/3)\tilde{S}_{ij}^{(2D)}/N$, $o_{ij} \equiv \Omega_{ij}/N$ and $\tilde{m}_{ij} \equiv \beta_m M_{ij}^{(2D)}/N$, the algebraic relation reads

$$\boldsymbol{a} = -(\tilde{\boldsymbol{s}} + \tilde{\boldsymbol{m}}) + (\boldsymbol{a}\boldsymbol{o} - \boldsymbol{o}\boldsymbol{a}) - \beta(\boldsymbol{a}\tilde{\boldsymbol{s}} + \tilde{\boldsymbol{s}}\boldsymbol{a} - II_{a\tilde{s}}\boldsymbol{I}), \quad II_{a\tilde{s}} = tr\{\boldsymbol{a}\tilde{\boldsymbol{s}}\}, \quad \beta = \frac{C_2}{C_1 + \frac{2}{3}\beta_{w0}C_2} \tag{52}$$

Following Grigoriev and Lazeroms [20], the above relation can also be written as

$$\tilde{\boldsymbol{a}} = -\check{\boldsymbol{s}} + (\tilde{\boldsymbol{a}}\boldsymbol{o_1} - \boldsymbol{o_2}\tilde{\boldsymbol{a}}) \tag{53}$$

with:

$$\tilde{\boldsymbol{a}} = \frac{\boldsymbol{a} - \beta II_{a\tilde{s}}\boldsymbol{I}}{1 + 2\beta^2 II_{a\tilde{s}}} \tag{54}$$

$$\check{\boldsymbol{s}} = \tilde{\boldsymbol{s}} + \frac{\tilde{\boldsymbol{m}}}{1 + 2\beta^2 II_{a\tilde{s}}} \tag{55}$$

$$\boldsymbol{o_1} = \boldsymbol{o} - \beta\tilde{\boldsymbol{s}} \tag{56}$$

$$\boldsymbol{o_2} = \boldsymbol{o} + \beta\tilde{\boldsymbol{s}} \tag{57}$$

Eq. 53 looks like the simplified algebraic relation obtained by Wallin and Johansson [18] with $c_2 = 5/9$ except that the relation is written for a non-traceless pseudo-anisotropy tensor and that tensors $\boldsymbol{o_1}$ and $\boldsymbol{o_2}$ are no longer antisymmetric, contrary to the single tensor $\boldsymbol{o}$. However, the developments to obtain an explicit algebraic relation remain mainly the same. Hence, the first step consists in writing the first recursive usage of the implicit relation, Eq. 53, leading to

$$\tilde{\boldsymbol{a}} = -\check{\boldsymbol{s}} - (\check{\boldsymbol{s}}\boldsymbol{o_1} - \boldsymbol{o_2}\check{\boldsymbol{s}}) + (\tilde{\boldsymbol{a}}\boldsymbol{o_1}^2 + \boldsymbol{o_2}^2\tilde{\boldsymbol{a}} - 2\boldsymbol{o_2}\tilde{\boldsymbol{a}}\boldsymbol{o_1}) \tag{58}$$

In order to express the last term in the right hand side of the above relation, the implicit relation Eq. 53 is again recursively employed to obtain:

$$\begin{aligned} \boldsymbol{o_2}\tilde{\boldsymbol{a}}\boldsymbol{o_1} &= -\boldsymbol{o_2}\check{\boldsymbol{s}}\boldsymbol{o_1} + \boldsymbol{o_2}\tilde{\boldsymbol{a}}\boldsymbol{o_1}^2 - \boldsymbol{o_2}^2\tilde{\boldsymbol{a}}\boldsymbol{o_1} \\ &= -\boldsymbol{o_2}\check{\boldsymbol{s}}\boldsymbol{o_1} - (\check{\boldsymbol{s}} + \tilde{\boldsymbol{a}} - \tilde{\boldsymbol{a}}\boldsymbol{o_1})\boldsymbol{o_1}^2 - \boldsymbol{o_2}^2(\check{\boldsymbol{s}} + \tilde{\boldsymbol{a}} + \boldsymbol{o_2}\tilde{\boldsymbol{a}}) \end{aligned} \tag{59}$$

This leads to the following relation:

$$\boldsymbol{o_2}\tilde{\boldsymbol{a}}\boldsymbol{o_1} + \tilde{\boldsymbol{a}}\boldsymbol{o_1}^2 + \boldsymbol{o_2}^2\tilde{\boldsymbol{a}} = -\boldsymbol{o_2}\check{\boldsymbol{s}}\boldsymbol{o_1} - \check{\boldsymbol{s}}\boldsymbol{o_1}^2 - \boldsymbol{o_2}^2\check{\boldsymbol{s}} + \tilde{\boldsymbol{a}}\boldsymbol{o_1}^3 - \boldsymbol{o_2}^3\tilde{\boldsymbol{a}} \tag{60}$$

Hence, this allows to write Eq. 58 as:

$$\tilde{\boldsymbol{a}} = -\check{\boldsymbol{s}} - (\check{\boldsymbol{s}}\boldsymbol{o_1} - \boldsymbol{o_2}\check{\boldsymbol{s}}) + 3(\tilde{\boldsymbol{a}}\boldsymbol{o_1}^2 + \boldsymbol{o_2}^2\tilde{\boldsymbol{a}}) + 2(\boldsymbol{o_2}\check{\boldsymbol{s}}\boldsymbol{o_1} + \check{\boldsymbol{s}}\boldsymbol{o_1}^2 + \boldsymbol{o_2}^2\check{\boldsymbol{s}} - \tilde{\boldsymbol{a}}\boldsymbol{o_1}^3 + \boldsymbol{o_2}^3\tilde{\boldsymbol{a}}) \tag{61}$$

In order to simplify the last two terms in brackets involved in the above relation, using the Cayley-Hamilton theorem for a two-dimensional traceless tensor Eq. 131 and recalling that $\boldsymbol{o}$ is antisymmetric and $\tilde{\boldsymbol{s}}$ is symmetric, one gets:

$$\boldsymbol{o_1}^2 = \boldsymbol{o_2}^2 = \frac{1}{2}\left(II_o + \beta^2 II_{\tilde{s}}\right)\boldsymbol{I} \tag{62}$$

As a result, inserting these expressions in Eq. 61 leads to:

$$\tilde{\boldsymbol{a}} = -\check{\boldsymbol{s}} - (\check{\boldsymbol{s}}\boldsymbol{o_1} - \boldsymbol{o_2}\check{\boldsymbol{s}}) + 3\left(II_o + \beta^2 II_{\tilde{s}}\right)\tilde{\boldsymbol{a}} + 2\left(\boldsymbol{o_2}\check{\boldsymbol{s}}\boldsymbol{o_1} + \left(II_o + \beta^2 II_{\tilde{s}}\right)\left(\check{\boldsymbol{s}} - \frac{1}{2}\left(\tilde{\boldsymbol{a}}\boldsymbol{o_1} - \boldsymbol{o_2}\tilde{\boldsymbol{a}}\right)\right)\right) \tag{63}$$

Hence, using Eq. 53 to simplify the last term in the above expression leads to:

$$\left(1-2\left(II_o+\beta^2 II_{\tilde{s}}\right)\right)\tilde{\boldsymbol{a}} = -\left(1-\left(II_o+\beta^2 II_{\tilde{s}}\right)\right)\check{\boldsymbol{s}} - (\check{\boldsymbol{s}}\boldsymbol{o_1}-\boldsymbol{o_2}\check{\boldsymbol{s}}) + 2\boldsymbol{o_2}\check{\boldsymbol{s}}\boldsymbol{o_1} \tag{64}$$

Substituting the expressions for $o_1$, $o_2$ and $\check{s}$ in the second term on the right hand side of the above relation and using Eq. 131 leads to:

$$\check{\boldsymbol{s}}\boldsymbol{o_1}-\boldsymbol{o_2}\check{\boldsymbol{s}} = \tilde{\boldsymbol{s}}\boldsymbol{o}-\boldsymbol{o}\tilde{\boldsymbol{s}} - \beta II_{\tilde{s}}\boldsymbol{I} + \frac{1}{1+2\beta^2 II_{a\tilde{s}}}\left(\tilde{\boldsymbol{m}}\boldsymbol{o}-\boldsymbol{o}\tilde{\boldsymbol{m}} - \beta II_{\tilde{s}\tilde{m}}\boldsymbol{I}\right) \tag{65}$$

On the other hand, inserting the expressions for $o_1$ and $o_2$ in the last term on the right hand side of Eq. 61 leads to:

$$\boldsymbol{o_2}\check{\boldsymbol{s}}\boldsymbol{o_1} = \boldsymbol{o}\check{\boldsymbol{s}}\boldsymbol{o} + \beta(\tilde{\boldsymbol{s}}\check{\boldsymbol{s}}\boldsymbol{o}-\boldsymbol{o}\check{\boldsymbol{s}}\tilde{\boldsymbol{s}}) - \beta^2\tilde{\boldsymbol{s}}\check{\boldsymbol{s}}\tilde{\boldsymbol{s}} \tag{66}$$

The first and the last terms on the right hand side of the above relation can be simplified using Eq. 132 which is a consequence of the Cayley-Hamilton theorem for two arbitrary two-dimensional traceless tensors. Hence, from Eq. 132, the tensors $\boldsymbol{o}$ and $\check{\boldsymbol{s}}$ being antisymmetric and symmetric respectively, one obtains:

$$\boldsymbol{o}\check{\boldsymbol{s}}\boldsymbol{o} = -\frac{II_o}{2}\left(\tilde{\boldsymbol{s}} + \frac{\tilde{\boldsymbol{m}}}{1+2\beta^2 II_{a\tilde{s}}}\right) \tag{67}$$

$$\tilde{\boldsymbol{s}}\check{\boldsymbol{s}}\tilde{\boldsymbol{s}} = \left(\frac{II_{\tilde{s}}}{2} + \frac{II_{\tilde{m}\tilde{s}}}{1+2\beta^2 II_{a\tilde{s}}}\right)\tilde{\boldsymbol{s}} - \frac{II_{\tilde{s}}}{2}\frac{\tilde{\boldsymbol{m}}}{1+2\beta^2 II_{a\tilde{s}}} \tag{68}$$

Finally, moving on the term in brackets on the right hand side of Eq. 66, we first note that $\check{s}$ being symmetric and $o$ being antisymmetric, one gets:

$$\boldsymbol{o}\check{\boldsymbol{s}} + \check{\boldsymbol{s}}\boldsymbol{o} = 0 \tag{69}$$

Hence from left and right multiplication of Eq. 69 by $\tilde{\boldsymbol{s}}$, one obtains:

$$\tilde{\boldsymbol{s}}\check{\boldsymbol{s}}\boldsymbol{o}-\boldsymbol{o}\check{\boldsymbol{s}}\tilde{\boldsymbol{s}} = \check{\boldsymbol{s}}\boldsymbol{o}\tilde{\boldsymbol{s}} - \tilde{\boldsymbol{s}}\boldsymbol{o}\check{\boldsymbol{s}} = \frac{1}{1+2\beta^2 II_{a\tilde{s}}}(\tilde{\boldsymbol{m}}\boldsymbol{o}\tilde{\boldsymbol{s}} - \tilde{\boldsymbol{s}}\boldsymbol{o}\tilde{\boldsymbol{m}}) \tag{70}$$

Using again Eq. 131 with $\boldsymbol{a} = \tilde{\boldsymbol{s}}\boldsymbol{o}$ and $\boldsymbol{b} = \tilde{\boldsymbol{m}}$ and recalling that as $\tilde{\boldsymbol{m}}$ is symmetric and $\boldsymbol{o}$ is antisymmetric, one has $\tilde{\boldsymbol{s}}\boldsymbol{o} = -\boldsymbol{o}\tilde{\boldsymbol{s}}$, yields:

$$\tilde{\boldsymbol{s}}\check{\boldsymbol{s}}\boldsymbol{o}-\boldsymbol{o}\check{\boldsymbol{s}}\tilde{\boldsymbol{s}} = \frac{-III_{\tilde{s}o\tilde{m}}}{1+2\beta^2 II_{a\tilde{s}}}\boldsymbol{I} \tag{71}$$

Hence, collecting the results, the algebraic relation reads:

$$\begin{aligned}\left(1-2\left(II_o+\beta^2 II_{\tilde{s}}\right)\right)\tilde{\boldsymbol{a}} = &-\left(1+\frac{2\beta^2 II_{\tilde{m}\tilde{s}}}{1+2\beta^2 II_{a\tilde{s}}}\right)\tilde{\boldsymbol{s}} - \left(\frac{1-2\beta^2 II_{\tilde{s}}}{1+2\beta^2 II_{a\tilde{s}}}\right)\tilde{\boldsymbol{m}} \\ &- (\tilde{\boldsymbol{s}}\boldsymbol{o}-\boldsymbol{o}\tilde{\boldsymbol{s}}) - \frac{1}{1+2\beta^2 II_{a\tilde{s}}}(\tilde{\boldsymbol{m}}\boldsymbol{o}-\boldsymbol{o}\tilde{\boldsymbol{m}}) \\ &+ \beta\left(II_{\tilde{s}} - \frac{2III_{\tilde{s}o\tilde{m}} - II_{\tilde{m}\tilde{s}}}{1+2\beta^2 II_{a\tilde{s}}}\right)\boldsymbol{I}\end{aligned} \tag{72}$$

Taking the trace of the above algebraic relation allows to obtain directly an explicit expression for $II_{a\tilde{s}}$ that reads:

$$II_{a\tilde{s}} = \frac{2III_{\tilde{s}o\tilde{m}} - II_{\tilde{m}\tilde{s}} - II_{\tilde{s}}}{1-2II_o} \tag{73}$$

Finally, the explicit algebraic relation for the anisotropy tensor writes:

$$\frac{1-2\left(II_o+\beta^2 II_{\tilde{s}}\right)}{1+2\beta^2 II_{a\tilde{s}}}\boldsymbol{a} = -\check{\boldsymbol{s}}-(\check{\boldsymbol{s}}\boldsymbol{o}-\boldsymbol{o}\check{\boldsymbol{s}}) + \frac{2\beta^2}{1+2\beta^2 II_{a\tilde{s}}}\left(II_{\tilde{s}}\tilde{\boldsymbol{m}}-II_{\tilde{m}\tilde{s}}\tilde{\boldsymbol{s}}\right) \tag{74}$$

While the above relation extents previous formulations that use a truncated integrity basis [14, 15], the introduction of elliptic blending results here in an algebraic relation that remains formally similar to the standard expression based on a linear pressure-strain model [18] except the last term on the right hand side of Eq. 74. As in [14, 15], the introduction of elliptic blending results further from Eq. 73 and 74 in the appearance of the two additional invariants $II_{SM^{(2D)}}$ and $III_{S\Omega M^{(2D)}}$ that both characterize the velocity gradient in the coordinate system linked to the wall. The new invariant $II_{SM^{(2D)}}$ refers to an impingement invariant as it reaches its maximum value at an impingement point while it is zero when the flow is parallel to the wall. The maximum value corresponds either to $II^2_{SM^{(2D)}}/II_S = 1/2$ for a two-dimensional impingement point or $II^2_{SM^{(2D)}}/II_S = 2/3$ for an axisymmetric impingement point. On the other hand, $III_{S\Omega M^{(2D)}}$ refers to a boundary layer invariant as it is zero at an impingement point while it reaches its maximum value $III_{S\Omega M^{(2D)}} = II_S/2$ when the flow is parallel to the wall.

### 2.4 Explicit algebraic model for three-dimensional mean flows

For three-dimensional mean flows, introducing $\tilde{s} \equiv C_1\tilde{S}_{ij}/N$, $o \equiv \Omega_{ij}/N$ and $\tilde{m} \equiv \beta_m M_{ij}/N$, the algebraic relation Eq. 32 reads

$$\boldsymbol{a} = -(\tilde{\boldsymbol{s}}+\tilde{\boldsymbol{m}}) + (\boldsymbol{a}\boldsymbol{o}-\boldsymbol{o}\boldsymbol{a}) - \beta(\boldsymbol{a}\tilde{\boldsymbol{s}}+\tilde{\boldsymbol{s}}\boldsymbol{a}-\frac{2}{3}II_{a\tilde{s}}\boldsymbol{I}), \quad II_{a\tilde{s}} = tr\{\boldsymbol{a}\tilde{\boldsymbol{s}}\}, \quad \beta = \frac{C_2}{C_1} \tag{75}$$

As for two-dimensional mean flows, the above relation can also be written as in [20]:

$$\tilde{\boldsymbol{a}} = -\check{\boldsymbol{s}} + (\tilde{\boldsymbol{a}}\boldsymbol{o_1}-\boldsymbol{o_2}\tilde{\boldsymbol{a}}) \tag{76}$$

with :

$$\tilde{\boldsymbol{a}} = \frac{\boldsymbol{a}-\frac{2}{3}\beta II_{a\tilde{s}}\boldsymbol{I}}{1+\frac{4}{3}\beta^2 II_{a\tilde{s}}} \tag{77}$$

$$\check{\boldsymbol{s}} = \tilde{\boldsymbol{s}} + \frac{\tilde{\boldsymbol{m}}}{1+\frac{4}{3}\beta^2 II_{a\tilde{s}}} \tag{78}$$

$$\boldsymbol{o_1} = \boldsymbol{o}-\beta\tilde{\boldsymbol{s}} \tag{79}$$

$$\boldsymbol{o_2} = \boldsymbol{o}+\beta\tilde{\boldsymbol{s}} \tag{80}$$

Here again, the above relation Eq. 76 for three-dimensional mean flows looks like the algebraic relation Eq. 53 obtained for two-dimensional mean flows and the developments to obtain an explicit algebraic relation will remain mainly the same. Hence, the first step consists in writing the first recursive usage of the implicit relation, Eq. 76, leading to

$$\tilde{\boldsymbol{a}} = -\check{\boldsymbol{s}} - (\check{\boldsymbol{s}}\boldsymbol{o_1}-\boldsymbol{o_2}\check{\boldsymbol{s}}) + (\tilde{\boldsymbol{a}}\boldsymbol{o_1}^2+\boldsymbol{o_2}^2\tilde{\boldsymbol{a}}-2\boldsymbol{o_2}\tilde{\boldsymbol{a}}\boldsymbol{o_1}) \tag{81}$$

In order to express the last term in brackets on the right hand side of the above relation, the recursive usage of the implicit relation Eq. 76 is again employed to obtain:

$$\begin{aligned}\boldsymbol{o_2}\tilde{\boldsymbol{a}}\boldsymbol{o_1} &= -\boldsymbol{o_2}\check{\boldsymbol{s}}\boldsymbol{o_1}+\boldsymbol{o_2}\tilde{\boldsymbol{a}}\boldsymbol{o_1}^2-\boldsymbol{o_2}^2\tilde{\boldsymbol{a}}\boldsymbol{o_1} \\ &= -\boldsymbol{o_2}\check{\boldsymbol{s}}\boldsymbol{o_1}-(\check{\boldsymbol{s}}+\tilde{\boldsymbol{a}}-\tilde{\boldsymbol{a}}\boldsymbol{o_1})\boldsymbol{o_1}^2-\boldsymbol{o_2}^2(\check{\boldsymbol{s}}+\tilde{\boldsymbol{a}}+\boldsymbol{o_2}\tilde{\boldsymbol{a}})\end{aligned} \tag{82}$$

This leads to the following relation:

$$\boldsymbol{o_2\tilde{a}o_1} + \boldsymbol{\tilde{a}o_1}^2 + \boldsymbol{o_2}^2\boldsymbol{\tilde{a}} = -\boldsymbol{o_2\check{s}o_1} - \boldsymbol{\check{s}o_1}^2 - \boldsymbol{o_2}^2\boldsymbol{\check{s}} + \boldsymbol{\tilde{a}o_1}^3 - \boldsymbol{o_2}^3\boldsymbol{\tilde{a}} \tag{83}$$

Hence, this allows to write Eq. 81 as:

$$\boldsymbol{\tilde{a}} = -\boldsymbol{\check{s}} - (\boldsymbol{\check{s}o_1} - \boldsymbol{o_2\check{s}}) - (\boldsymbol{o_2\check{s}o_1} + \boldsymbol{\check{s}o_1}^2 + \boldsymbol{o_2}^2\boldsymbol{\check{s}} - \boldsymbol{\tilde{a}o_1}^3 + \boldsymbol{o_2}^3\boldsymbol{\tilde{a}} + 3\boldsymbol{o_2\tilde{a}o_1}) \tag{84}$$

In order to simplify the last term in brackets involved in the above relation, using the Cayley-Hamilton theorem for a three-dimensional traceless tensor Eqs. 136-139 and recalling that $\boldsymbol{o}$ is antisymmetric and $\tilde{\boldsymbol{s}}$ is symmetric, yields:

$$\boldsymbol{o_1}^3 = \frac{1}{2}II_\beta\boldsymbol{o_1} - \beta III_\beta\boldsymbol{I} \tag{85}$$

$$\boldsymbol{o_2}^3 = \frac{1}{2}II_\beta\boldsymbol{o_2} + \beta III_\beta\boldsymbol{I} \tag{86}$$

where similar notations as introduced in [20], are adopted:

$$II_\beta = II_o + \beta^2 II_{\tilde{s}} \tag{87}$$

$$III_\beta = III_{\tilde{s}o^2} + \frac{\beta^2}{3}III_{\tilde{s}} \tag{88}$$

As a result, inserting these expressions in Eq. 84 leads to:

$$\begin{aligned}\boldsymbol{\tilde{a}} = &-\boldsymbol{\check{s}} - (\boldsymbol{\check{s}o_1} - \boldsymbol{o_2\check{s}}) - (\boldsymbol{o_2\check{s}o_1} + \boldsymbol{\check{s}o_1}^2 + \boldsymbol{o_2}^2\boldsymbol{\check{s}}) \\ &+ \frac{1}{2}II_\beta(\boldsymbol{\tilde{a}o_1} - \boldsymbol{o_2\tilde{a}}) - 2\beta III_\beta\boldsymbol{\tilde{a}} - 3\boldsymbol{o_2\tilde{a}o_1}\end{aligned} \tag{89}$$

Hence, the use of Eq. 76 allows to obtain the following relation:

$$\begin{aligned}\left(1 - \frac{1}{2}II_\beta + 2\beta III_\beta\right)\boldsymbol{\tilde{a}} = &-\left(1 - \frac{1}{2}II_\beta\right)\boldsymbol{\check{s}} - (\boldsymbol{\check{s}o_1} - \boldsymbol{o_2\check{s}}) \\ &- (\boldsymbol{o_2\check{s}o_1} + \boldsymbol{\check{s}o_1}^2 + \boldsymbol{o_2}^2\boldsymbol{\check{s}}) - 3\boldsymbol{o_2\tilde{a}o_1}\end{aligned} \tag{90}$$

In order to express the last term in the above relation, the recursive usage of the implicit relation is invoked again, leading to:

$$\boldsymbol{o_2\tilde{a}o_1} = \boldsymbol{o_2}(-\boldsymbol{\check{s}} - \boldsymbol{\check{s}o_1} + \boldsymbol{o_2\check{s}})\boldsymbol{o_1} + \boldsymbol{o_2}(\boldsymbol{\tilde{a}o_1}^2 - 2\boldsymbol{o_2\tilde{a}o_1} + \boldsymbol{o_2}^2\boldsymbol{\tilde{a}})\boldsymbol{o_1} \tag{91}$$

The use of Eq. 83 allows to express the last term of Eq. 91 as:

$$\begin{aligned}\boldsymbol{o_2}(\boldsymbol{\tilde{a}o_1}^2 - 2\boldsymbol{o_2\tilde{a}o_1} + \boldsymbol{o_2}^2\boldsymbol{\tilde{a}})\boldsymbol{o_1} &= 3\boldsymbol{o_2}(\boldsymbol{\tilde{a}o_1}^2 + \boldsymbol{o_2}^2\boldsymbol{\tilde{a}})\boldsymbol{o_1} - 2\boldsymbol{o_2}(\boldsymbol{\tilde{a}o_1}^2 + \boldsymbol{o_2\tilde{a}o_1} + \boldsymbol{o_2}^2\boldsymbol{\tilde{a}})\boldsymbol{o_1} \\ &= 3\boldsymbol{o_2\tilde{a}o_1}^3 + 3\boldsymbol{o_2}^3\boldsymbol{\tilde{a}o_1} - 2\boldsymbol{o_2}(-\boldsymbol{o_2\check{s}o_1} - \boldsymbol{\check{s}o_1}^2 - \boldsymbol{o_2}^2\boldsymbol{\check{s}} + \boldsymbol{\tilde{a}o_1}^3 - \boldsymbol{o_2}^3\boldsymbol{\tilde{a}})\boldsymbol{o_1}\end{aligned} \tag{92}$$

Using Eqs. 85-86 together with the implicit relation to remove the products $\boldsymbol{\tilde{a}o_1} - \boldsymbol{o_2\tilde{a}}$, one gets:

$$\begin{aligned}\boldsymbol{o_2}(\boldsymbol{\tilde{a}o_1}^2 - 2\boldsymbol{o_2\tilde{a}o_1} + \boldsymbol{o_2}^2\boldsymbol{\tilde{a}})\boldsymbol{o_1} = &(2II_\beta + 4\beta III_\beta)\,\boldsymbol{o_2\tilde{a}o_1} \\ &- \boldsymbol{2o_2}\left(-\boldsymbol{o_2\check{s}o_1} - \boldsymbol{\check{s}o_1}^2 - \boldsymbol{o_2}^2\boldsymbol{\check{s}} + \frac{1}{2}II_\beta\boldsymbol{\check{s}}\right)\boldsymbol{o_1} \\ &+ 3\beta III_\beta(\boldsymbol{\tilde{a}} + \boldsymbol{\check{s}})\end{aligned} \tag{93}$$

This can be further simplified by using again Eqs. 85-86:

$$\begin{aligned}\boldsymbol{o_2}(\tilde{\boldsymbol{a}}\boldsymbol{o_1}^2 - 2\boldsymbol{o_2}\tilde{\boldsymbol{a}}\boldsymbol{o_1} + \boldsymbol{o_2}^2\tilde{\boldsymbol{a}})\boldsymbol{o_1} = &(2II_\beta + 4\beta III_\beta)\,\boldsymbol{o_2}\tilde{\boldsymbol{a}}\boldsymbol{o_1} \\ &+ \boldsymbol{o_2}\,(2\boldsymbol{o_2}\check{\boldsymbol{s}}\boldsymbol{o_1} + II_\beta\check{\boldsymbol{s}})\,\boldsymbol{o_1} + 2\beta III_\beta(\check{\boldsymbol{s}}\boldsymbol{o_1} - \boldsymbol{o_2}\check{\boldsymbol{s}}) \\ &+ 3\beta III_\beta(\tilde{\boldsymbol{a}} + \check{\boldsymbol{s}})\end{aligned} \tag{94}$$

Hence, collecting the results from Eqs. 91 and 94, one obtains:

$$\begin{aligned}(1 - 2II_\beta - 4\beta III_\beta)\,\boldsymbol{o_2}\tilde{\boldsymbol{a}}\boldsymbol{o_1} = &\boldsymbol{o_2}\,(2\boldsymbol{o_2}\check{\boldsymbol{s}}\boldsymbol{o_1} - (1 - II_\beta)\,\check{\boldsymbol{s}} - \check{\boldsymbol{s}}\boldsymbol{o_1} + \boldsymbol{o_2}\check{\boldsymbol{s}}\boldsymbol{o_1}) \\ &+ 2\beta III_\beta(\check{\boldsymbol{s}}\boldsymbol{o_1} - \boldsymbol{o_2}\check{\boldsymbol{s}}) + 3\beta III_\beta(\tilde{\boldsymbol{a}} + \check{\boldsymbol{s}})\end{aligned} \tag{95}$$

The resulting system to be solved thus consists of Eqs. 90 and 95. Hence, multiplying Eq. 90 by $(1 - 2II_\beta - 4\beta III_\beta)$ and using Eq. 95 leads to the following explicit algebraic relation:

$$\begin{aligned}Q\tilde{\boldsymbol{a}} = &-\left[Q_0\left(1 - \frac{1}{2}II_\beta\right) + 9\beta III_\beta\right]\check{\boldsymbol{s}} \\ &- (1 - 2II_\beta + 2\beta III_\beta)\,(\check{\boldsymbol{s}}\boldsymbol{o_1} - \boldsymbol{o_2}\check{\boldsymbol{s}}) - Q_0\left(\check{\boldsymbol{s}}\boldsymbol{o_1}^2 + \boldsymbol{o_2}^2\check{\boldsymbol{s}}\right) \\ &+ 2Q_1\boldsymbol{o_2}\check{\boldsymbol{s}}\boldsymbol{o_1} - 3\boldsymbol{o_2}\,(2\boldsymbol{o_2}\check{\boldsymbol{s}}\boldsymbol{o_1} - \check{\boldsymbol{s}}\boldsymbol{o_1} + \boldsymbol{o_2}\check{\boldsymbol{s}}\boldsymbol{o_1})\end{aligned} \tag{96}$$

with

$$Q_0 = 1 - 2II_\beta - 4\beta III_\beta \tag{97}$$

$$Q_1 = 1 - \frac{1}{2}II_\beta + 2\beta III_\beta \tag{98}$$

$$Q = Q_0Q_1 + 9\beta III_\beta \tag{99}$$

As in the two-dimensional case, taking the trace of the above relation allows to obtain directly an explicit expression for $II_{a\tilde{s}}$ that reads:

$$II_{a\tilde{s}} = \frac{-(\Delta_1 + \Delta_2)}{Q + \frac{4}{3}\beta^2\Delta_1} \tag{100}$$

with:

$$\Delta_1 = II_{\tilde{s}}\left(1 - \frac{7}{2}II_\beta\right) + 6III_\beta^2 + 6IV_{\tilde{s}^2o^2} - 2\beta\,(III_{\tilde{s}} - II_{\tilde{s}}III_\beta) + 3\beta^2II_{\tilde{s}}^2 \tag{101}$$

$$\begin{aligned}\Delta_2 = &(1 - 2II_\beta + 2\beta III_\beta)\,(II_{\tilde{m}\tilde{s}} - 2III_{\tilde{s}o\tilde{m}}) - 3\,(2V_{o^2\tilde{s}o\tilde{m}} + IV_{o\tilde{s}o\tilde{m}} - 2III_{\tilde{m}o^2}III_\beta) \\ &+ \beta\,[3III_{\tilde{m}o^2}II_{\tilde{s}} - 2III_{\tilde{m}s^2}\,(1 - 2II_\beta) + 3\,(-4V_{\tilde{s}^2o^2\tilde{m}} + II_{\tilde{m}\tilde{s}}III_{\tilde{s}o^2} + 2IV_{\tilde{s}^2o\tilde{m}})] \\ &\beta^2\left[6V_{\tilde{s}o\tilde{s}^2\tilde{m}} + 3II_{\tilde{s}}\left(\frac{1}{2}II_{\tilde{m}\tilde{s}} - 2III_{\tilde{s}o\tilde{m}}\right) + 2III_{\tilde{m}\tilde{s}^2}III_\beta\right] \\ &+ \beta^3\,[III_{\tilde{s}}II_{\tilde{m}\tilde{s}} + 3III_{\tilde{m}\tilde{s}^2}II_{\tilde{s}}]\end{aligned} \tag{102}$$

### 2.5 Solution of the explicit algebraic model

The previous algebraic relations, Eq. 74 for two-dimensional mean flows or Eq. 96 for three-dimensional mean flows, involves coefficients that require, as usual in the derivation of explicit algebraic models, the determination of $N$ or, equivalently, the production-to-dissipation ratio. The nonlinear equation for $N$ is derived by introducing the solution of $a_{ij}$ given by either Eq. 74 or Eq. 96 in $II_{aS}$ for the definition of $N$.

Far from the wall, substituting $C_2 = 0$, one gets the same nonlinear equation for $N$ as Wallin and Johansson [18]. In this case, the equation is cubic in the two-dimensional case and an analytical solution is available. Unfortunately, in the general case, the polynomial equation for $N$ is of small interest as there is no obvious analytical solution. As discussed by Lazeroms *et. al* [21], different strategies have been followed to solve this issue. One possible strategy consists in prescribing a constant equilibrium value of the production-to-dissipation ratio. While this greatly simplifies the problem, this leads to an inconsistent formulation in flow situations where the ratio deviates from its equilibrium value. Another promising strategy consists in finding the best possible analytical expression that approximates the fully consistent formulation. This strategy may further be complemented by a reduced number of iterations to obtain a self-consistent formulation. We follow in this work this strategy by providing an approximate nonlinear equation for $N$ in the two-dimensional case, and for which an analytical solution can be found.

### 2.5.1 Solution for two-dimensional impinging or parallel shear flows

In the two-dimensional case, as $II_{a\tilde{s}}$ is already known from Eq. 73, only the expression for $II_{a\tilde{m}}$ is required to express $II_{aS}$. This can be done by right multiplying the algebraic relation Eq. 74 by $\tilde{m}$ and taking the trace of the result, and leads to:

$$\begin{aligned}\left(1 - 2\left(II_o + \beta^2 II_{\tilde{s}}\right)\right) II_{a\tilde{m}} = &- \left(1 + 2\beta^2 II_{a\tilde{s}}\right)\left(2III_{\tilde{s}o\tilde{m}} + II_{\tilde{m}\tilde{s}}\right) \\ &+ 2\beta^2\left(II_{\tilde{s}} II_{\tilde{m}} - II^2_{\tilde{m}\tilde{s}}\right) - II_{\tilde{m}}\end{aligned} \tag{103}$$

Hence, substituting $s \equiv (C_1 + 2\beta_{w0}C_2/3)\tilde{S}_{ij}/N$, $\tilde{m} \equiv \beta_m M_{ij}^{(2D)}/N$ and $o \equiv \Omega_{ij}/N$ in the above relations leads to the following expression for $II_{aS}$:

$$\begin{aligned}II_{aS} = &- \left(C_1 - \frac{4}{3}C_2\right)\frac{NII_S}{N^2 - 2II_\Omega} - \frac{C_2}{6}\frac{2 + \beta_{w0}}{N^2 - 2II_\Omega}\left(N\left(15II_{SM^{(2D)}} + 4II_S\right) - 30III_{S\Omega M^{(2D)}}\right) \\ &- \frac{3C_2^2}{4}\left(C_1 - \frac{4}{3}C_2\right)\frac{75}{Q\left(N^2 - 2II_\Omega\right)}\left(II_\Omega\left(II_M II_S - II^2_{SM^{(2D)}}\right) + 2III^2_{S\Omega M^{(2D)}}\right)\end{aligned} \tag{104}$$

where $\beta_{w0}$ is given by:

$$\beta_{w0} = \frac{-C_2}{Q}\left[5\left(N^2 - 2II_\Omega\right) + 2\beta_m\left(2III_{S\Omega M^{(2D)}} - NII_{S\tilde{M}^{(2D)}}\right) - 2NC_1 II_{\tilde{S}}\right] \tag{105}$$

The denominator $Q$ is expressed as:

$$Q = \left(N^2 - 2II_\Omega\right)(2N - 5C_2) - \frac{4}{3}NC_2^2 II_{\tilde{S}} \tag{106}$$

This results in the following sixth- order polynomial equation for $N$:

$$N^4 - c_2' N^3 - b_2 N^2 + b_1 N - b_0 - \frac{5}{4}C_2^2 C_3 \beta_m II_S \Lambda(N) = 0 \tag{107}$$

where the coefficients of the polynomial equation are given by:

$$b_2 = 2II_\Omega + \left(C_1 C_3 + \frac{2}{3}C_2^2\right) II_S + 5C_2\left(C_2 + C_3\right) II_{SM^{(2D)}} - \frac{5}{4}C_2\left(2c_1' - a_3 C_2\right) \tag{108}$$

$$\begin{aligned}b_1 = &2c_2' II_\Omega + C_2\left(\frac{2}{3}c_3' C_2 + \frac{5}{2}C_1 C_3\right) II_S \\ &+ \frac{5}{2}C_2\left(4C_3 III_{S\Omega M^{(2D)}} + 2C_2\left(c_1' + a_3 C_3\right) II_{SM^{(2D)}} + \frac{a_3}{2}c_1' C_2\right)\end{aligned} \tag{109}$$

$$b_0 = 5c_1' C_2 II_\Omega + 10 a_3 C_2^2 C_3 III_{S\Omega M^{(2D)}} \tag{110}$$

with

$$c_2' = c_1' + \frac{5}{2}C_2\,, \quad c_3' = c_1' + \frac{5}{2}C_3\,, \quad \Lambda(N) = \frac{2}{II_S}\frac{4III_{S\Omega M^{(2D)}}^2 - N^2\left(II_{MS}^2 - II_S II_M\right)}{N^2 - 2II_\Omega} \tag{111}$$

As already noticed, the introduction of elliptic blending results in the appearance of the two additional invariants $II_{SM^{(2D)}}$ and $III_{S\Omega M^{(2D)}}$. When the flow is parallel to the wall, $II_{SM^{(2D)}}$ is zero whereas $III_{S\Omega M^{(2D)}} = II_S/2$. On the other hand, at a two-dimensional impingement point, $III_{S\Omega M^{(2D)}}$ is zero while $II_{SM^{(2D)}}^2 = II_S/2$. Hence, recalling that $II_S = -II_\Omega$ for flows parallel to the wall, the above known values of the two new invariants indicate that $\Lambda(N) = 0$ for a two-dimensional impingement point whereas $\Lambda(N) = 1$ for a flow parallel to the wall. Hence, in both cases, the nonlinear equation reduces to a quartic equation. This is of particular practical interest as the above two flow situations are representative of near-wall two-dimensional flows.

Hence, by assuming that $\Lambda$ is a constant coefficient with either $\Lambda = 0$ or $\Lambda = 1$, dividing Eq. 107 by ${c_2'}^4$, the equation for $\tilde{N} = N/c_2'$ reads:

$$\tilde{N}^4 - \tilde{N}^3 - a\tilde{N}^2 - b\tilde{N} - c = 0 \tag{112}$$

where the coefficients of the polynomial equation are now given by:

$$a = b_2 {c_2'}^{-2}\,, \quad b = -b_1 {c_2'}^{-3}\,, \quad c = \left(b_0 + \frac{5}{4}C_2^2 C_3 \beta_m II_S \Lambda\right) {c_2'}^{-4} \tag{113}$$

On the basis of the analysis provided in appendix B, the physical root is given by:

$$\tilde{N} = \frac{1}{4} + \frac{1}{2}R_{1,2} + \frac{1}{2}\sqrt{\frac{1}{2} + a - z + R_{1,2} + \frac{2b - z}{R_{1,2}}}\,, \quad R_{1,2} = \pm\sqrt{\frac{1}{4} + a + z} \tag{114}$$

where the choice of $R_{1,2}$ is made to ensure a real root and $z$ is given by $z = (b^2 - c - 4ac)\hat{N}^{-1}/(b + 4c)$ with:

$$\hat{N} = \begin{cases} \dfrac{1}{3} + \left(P_1 + \sqrt{P_2}\right)^{1/3} + \text{sign}\left(P_1 - \sqrt{P_2}\right)|P_1 - \sqrt{P_2}|^{1/3} & P_2 \geq 0 \\ \dfrac{1}{3} + 2\sqrt{P}\cos\left(\dfrac{1}{3}\arccos\left(\dfrac{P_1}{P^{3/2}}\right)\right) & P_2 < 0 \end{cases} \tag{115}$$

with

$$P_2 = P_1^2 - P^3\,, \quad P = \frac{1 + 3A}{9}\,, \quad P_1 = \frac{1}{27}\left(1 + \frac{9}{2}A + \frac{27}{2}B\right) \tag{116}$$

### 2.5.2 Limiting behavior for two-dimensional mean flows parallel to the wall

For two-dimensional mean flows parallel to the wall, which is the case for fully developed channel flows, the expressions for the two-dimensional matrices reduce to:

$$S^{(2D)} = \begin{pmatrix} 0 & \sigma \\ \sigma & 0 \end{pmatrix}\,, \quad \Omega^{(2D)} = \begin{pmatrix} 0 & \sigma \\ -\sigma & 0 \end{pmatrix}\,, \quad M^{(2D)} = \begin{pmatrix} -1/2 & 0 \\ 0 & 1/2 \end{pmatrix} \tag{117}$$

The invariants simplify to $II_S = 2\sigma^2$, $II_\Omega = -2\sigma^2$, $II_{MS} = 0$ and $III_{SWM} = \sigma^2$, and the anisotropy tensor reads:

$$a = \begin{pmatrix} 2\sigma\eta_1 + N\eta_2 + \dfrac{\beta_w}{3} & -N\eta_1 + 2\sigma\eta_2 \\ -N\eta_1 + 2\sigma\eta_2 & -2\sigma\eta_1 - N\eta_2 + \dfrac{\beta_w}{3} \end{pmatrix}\,, \quad a_{33} = -\frac{2}{3}\beta_w \tag{118}$$

with:

$$\eta_1 = \frac{\sigma}{N^2+4\sigma^2}\left(C_1+\frac{2}{3}C_2\beta_w\right), \quad \eta_2 = \frac{15C_2\left(2+\beta_w\right)}{12\left(N^2+4\sigma^2\right)} \tag{119}$$

The coefficient $\beta_w$ reads:

$$\beta_w = \frac{6C_2\left(20\left(N^2+\left(4+4C_2-3C_1\right)\sigma^2\right)-N\left(75C_2+16\sigma^2C_1\right)\right)}{24\left(N^2+4\sigma^2\right)\left(5C_2-N\right)+N\left(225+64\sigma^2\right)C_2^2} \tag{120}$$

In the vicinity of the wall, the elliptic blending coefficient $\alpha$ tends to 0 and the equation for $N$ reduces to a cubic equation with coefficients $b_2 = -5a_3/4$, $b_1 = 5a_3^2/4$ and $b_0 = 0$. The solution for $N$ is provided in appendix B and reads $N = 15/4$. This value together with the limiting values $C_1 = 4/3$ and $C_2 = 1$ in the vicinity of the wall leads to the following limiting form

$$a = \begin{pmatrix} \frac{2}{3}\left(1+\beta_w\right) & 0 \\ 0 & -\frac{2}{3} \end{pmatrix}, \quad \beta_w = \frac{2}{5} - \frac{405}{450+128\sigma^2} \tag{121}$$

As the lower bound involved in the limitation procedure, Eq. 10, for the turbulent time scale, the dimensionless strain rate writes $\sigma = C_\tau/(2\sqrt{\varepsilon^+})$ with $\varepsilon^+ \simeq 0.23$ from channel flow DNS data leads to $\sigma = 6.25$ and $\beta = 0.325$. Hence, this reproduces the two-component limit of turbulence as $\overline{u_2'^2} \ll \overline{u_1'^2}$ and $\overline{u_2'^2} \ll \overline{u_3'^2}$. Moreover, the wall-normal component of the anisotropy tensor $a_{22} = -2/3$ is recovered while the predicted anisotropies $a_{11} = 0.88$ and $a_{33} = -0.21$ are close to channel flow DNS data.

It is worth mentioning that while it may be tempting to adopt a SSG-like model as proposed by Manceau [14] to improve the model performances in the log-layer, the limiting behavior may be drastically modified depending on the simplifications that have been made on the original SSG model. This is the case for instance for the SSG-like model assessed in this work which is obtained by adding the $b_3^*$-term and by approximating the $II_a$ invariant by $\sqrt{1-f}$. In this case, the adopted simplifications allow to follow the same methodology depicted previously to obtain an analytical solution for $N$ in the two-dimensional case but it can be shown that the above predicted anisotropies are strongly altered. This will be illustrated further in Section 4.1 in the frame of an a priori evaluation of the models performance.

### 2.5.3 General solution

As indicated previously, even in the case of two-dimensional mean flows, the polynomial equation for $N$ is of small interest as it is generally higher than fourth order and there is no obvious analytical solution. However, as noticed in [18], except in the vicinity of separation or a stagnation point, most of near-wall flows correspond to shear flows parallel to the wall and in this case an analytical solution is available. Hence, this means that the analytical solution provided in Sec. 2.5.1 is most of the time very close to the exact solution and is thus a good candidate for the initial guess of an iterative procedure. As usual, the iterative procedure that leads to a self-consistent model reads from the definition of $N$ as:

$$N_n = c_1' - C_3 a_{km}(N_{n-1})S_{km} \tag{122}$$

For the cases studied in this work, the method proves to be very robust and efficient and needs a small number of iterations, in practice $n \leq 3$.

# 3 Platform model

As usual for explicit algebraic models, the algebraic relation for the Reynolds-stress anisotropy tensor has to be complemented by transport equations for the turbulent kinetic energy $k$ and its dissipation rate $\varepsilon$ to close the turbulence model. In this work, the transport equation for $k$ reads as previously given by Eq. 25 without any dedicated additional near-wall terms while we adopt a transport equation for the dissipation rate which is very similar to the dissipation equation adopted in elliptic blending Reynolds-stress models [13]:

$$\frac{dk}{dt} = \mathcal{P} - \varepsilon + \frac{\partial}{\partial x_j}\left(\left(\nu + \frac{\nu_t}{\sigma_k}\right)\frac{\partial k}{\partial x_j}\right) \tag{123}$$

$$\frac{d\varepsilon}{dt} = \tau^{-1}\left(C'_{\varepsilon 1}\mathcal{P} - C_{\varepsilon 2}\varepsilon\right) + \frac{\partial}{\partial x_j}\left(\left(\nu + \frac{\nu_t}{\sigma_\varepsilon}\right)\frac{\partial \varepsilon}{\partial x_j}\right) \tag{124}$$

where $\tau$ is the turbulent time scale bounded by the Kolmogorov time scale as expressed by Eq. 10 and $C'_{\varepsilon 1}$ is a variable coefficient function of the production-to-dissipation ratio $\mathcal{P}/\varepsilon$ [8, 13] that aims at enhancing production of dissipation in the buffer layer

$$C'_{\varepsilon 1} = C_{\varepsilon 1}\left(1 + A_1\left(1 - f\right)\frac{\mathcal{P}}{\varepsilon}\right) \tag{125}$$

The modeling of the diffusion terms in the $k$ and $\varepsilon$ equations follows most of explicit algebraic models and is based on an eddy-viscosity modeling rather than on the Daly & Harlow model. In [18], the standard expression for the eddy-viscosity is adopted but with an effective $C_\mu$ evaluated as the proportional coefficient of the strain rate tensor of the algebraic relation. This definition seems very natural and it can be shown [22] that if the anisotropy tensor $a_{ij}$ is dependent only on the tensors $S_{ij}$ and $\Omega_{ij}$, the proportional coefficient can be expressed in the two-dimensional case as

$$C_\mu = -\frac{1}{2}\frac{II_{aS}}{II_S} \tag{126}$$

This relation is no longer valid here as the anisotropy tensor also depends on $M_{ij}$ but can be approximated by replacing $S_{ij}$ by $(C_1/N)\check{s}_{ij}$. While the use of an effective $C_\mu$ in the expression for the eddy-viscosity leads in practice to the correct near-wall behavior as reproduced by the Daly & Harlow model, it may also require the need of a specific calibration [23]. In order to avoid revisiting the model away from the walls, the use of a constant $C_\mu$ is adopted here as suggested in [24] together with a blending with a Daly & Harlow like model that produces the correct near-wall behavior [25]:

$$\nu_t = \left(f + (1-f)\frac{\overline{u'_i u'_j}}{k}n_i n_j\right)C_\mu \tau k \tag{127}$$

The standard set of constants $C_{\varepsilon 1}$, $C_{\varepsilon 2}$, $C_\mu$, $\sigma_k$ and $\sigma_\varepsilon$ is adopted without any recalibration procedure in such a way that the model predictions remain unaltered for far from the wall free-shear flows, their values are reported in Table 2. On the other hand, in Eq. 125, the constant $A_1$ needs to be calibrated. In practice, its value depends on the value of $C_L$ [5] and the values reported in Table 3 results from a calibration procedure on the basis of the fully developed turbulent channel flow case.

# 4 Model evaluation

This section aims at evaluating the model performances by comparison with DNS or large-eddy simulation data on fully developed wall-bounded turbulent flows. The first test case corresponds

| $C_{\varepsilon 1}$ | $C_{\varepsilon 2}$ | $\sigma_k$ | $\sigma_\varepsilon$ | $C_\mu$ |
|---|---|---|---|---|
| 1.44 | 1.92 | 1 | 1.3 | 0.09 |

Table 2: Platform model constants

to the fully developed turbulent channel flow that constitutes a classical corner stone case for assessing the performances of turbulence models with a dedicated near-wall treatment. The second test moves to a channel with rib roughness for which the mean flow remains two-dimensional but is no longer parallel to the wall and includes recirculation patterns. Finally, a three-dimensional case is addressed that consists in the fully developed turbulent flow in a square duct for which the corners are responsible for the anisotropy of Reynolds stress components and cause secondary motions. The computations are carried out using the open-source generic CFD solver library CALIF$^3$S (https://gforge.irsn.fr/gf/project/calif3s/). It uses a staggered finite volume discretization for which scalar unknowns are located at cell centers while the velocity is located at cell faces. Time discretization corresponds to a fractional step algorithm that consists in a pressure correction method. The numerical scheme corresponds to a centered second-order spatial discretization of both convective and diffusive fluxes together with the semi-implicit Crank-Nicolson time scheme [26]. The algebraic relation for the Reynolds stresses is discretized in time following the usual approach [18] that consists in introducing an effective $C_\mu$ coefficient defined by Eq. 126, but with $S_{ij}$ replaced by $(C_1/N)\check{s}_{ij}$, and adding the extra anisotropy contribution as fully explicit additional terms. For the above mentioned flow cases, the meshing is uniform along the streamwise direction, except for the channel with ribs, whereas a non-uniform meshing is used in the wall-normal direction(s) for which, denoting $h$ as the half-width, the transformation reads:

$$\forall k \in [1, N]\,, y_k = h\left[1 + \frac{1}{a}\tanh\left[\left(-1 + \frac{(k-1)}{N-1}\right)\tanh^{-1}(a)\right]\right]$$

According to the number of grid points $N$ in the wall-normal direction, the parameter $a$ is calculated by setting the first dimensionless grid point locations at $\delta^+ = 0.1$ with $\delta^+ = \delta \mathrm{Re}_\tau / h$.

### 4.1 A priori evaluation

In this section, before moving to the full model predictions, the algebraic relation is first tested with respect to DNS data [27] by performing a priori calculations for the fully turbulent channel flow case at two Reynolds numbers $\mathrm{Re}_\tau = 550$ and 2000. The mean velocity, turbulent kinetic energy and dissipation rate are taken from DNS data to compute the solution of the elliptic blending equation and then the Reynolds stresses given by the explicit algebraic relation. In addition, the production to dissipation ratio provided by the model is also compared with the ratio obtained from DNS data.

Table 3 shows the values for the model constants used for the a priori evaluation. The values have been calibrated from the fully developed turbulent channel flow case addressed in the upcoming section. As indicated previously, the adopted values for the $b_i$-coefficients of the homogeneous pressure-strain model are chosen to be equal to the corresponding values in the model of Wallin and Johansson [18], $b_1 = 1.8$, $b_3 = 4/5$, $b_4 = 1$ and $b_5 = 5/9$ together with $c_D = 2.6$ for the diffusion correction. This ensures the same behaviour far from the wall and allows a direct comparison. It must be noticed that, in order to focus on the elliptic blending features with respect to the standard homogeneous modeling, the near-wall treatments proposed in [18] are not taken into account in the

| | $C_L$ | $A_1$ |
|---|---|---|
| LRR - $f = \alpha^2$ | 0.07 | 0.03 |
| LRR - $f = \alpha^3$ | 0.055 | 0.1 |
| SSG - $f = \alpha^2$ | 0.135 | 0.11 |
| SSG - $f = \alpha^3$ | 0.095 | 0.15 |

Table 3: Model constants depending on the blending $f = \alpha^2$ or $f = \alpha^3$ and on the SSG-like correction $b_3^* = b_3$. The other model constants are $C_\eta = 80$ and $C_\tau = 6$

comparison. A slightly different version is also assessed through the use of a non-zero $b_3^*$-coefficient mimicking the SSG model in the near-wall region.

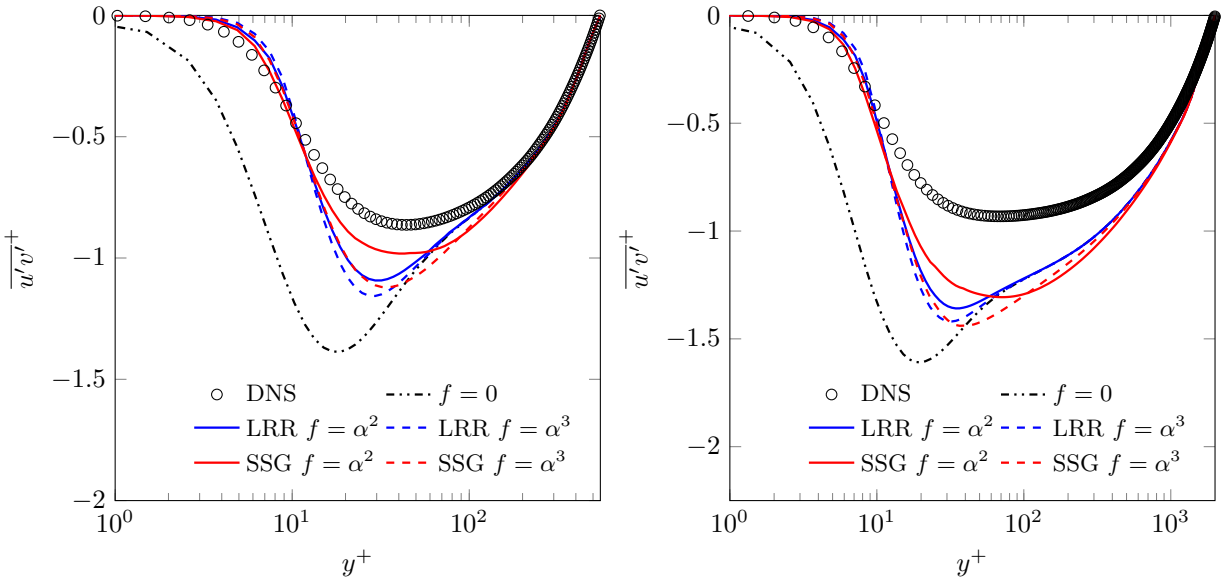


Figure 1: Turbulent channel flow. A priori test of the model for the shear component of the Reynolds stress at $\mathrm{Re}_\tau = 550$ (left) and $\mathrm{Re}_\tau = 2000$ (right)

Focusing first on the shear component of the Reynolds stress that constitutes the only component acting on the mean flow, Fig. 1 shows that the elliptic blending approach greatly improves the prediction of this component compared with the homogeneous model corresponding to $f = 0$. Contrary to what one would expect, the formulation $f = \alpha^2$ seems to slightly improve model predictions compared with $f = \alpha^3$ but the two formulations remain similar. Fig. 2 shows that the same conclusion can be drawn for the normal components reflecting the overall good behavior of the model, especially using the SSG-like correction that better reproduces the peaks in the buffer layer.

Recasting these results in terms of the anisotropies, Fig. 3 clearly shows that elliptic blending correctly predicts the decay of the $a_{12}$ anisotropy in the near wall region while the homogeneous model predicts a nearly constant value as already noticed in [18]. Some differences appear between LRR and SSG models in the log-layer but the anisotropies are fairly well predicted. Moving to the $a_{11}$, $a_{22}$ and $a_{33}$ anisotropies, Fig. 4 shows that as expected both LRR and SSG models recover the asymptotic value $a_{22} = -2/3$ for the wall-normal component whereas the asymptotic value for the streamwise

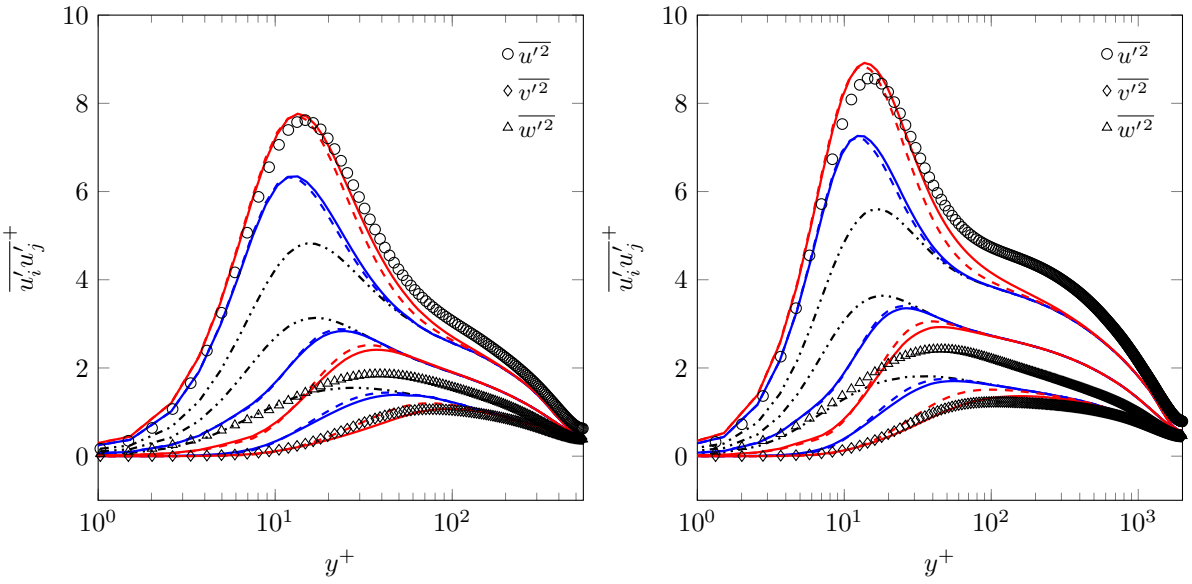


Figure 2: Turbulent channel flow. A priori test of the model for the normal component of the Reynolds stress at $\mathrm{Re}_\tau = 550$ (left) and $\mathrm{Re}_\tau = 2000$ (right). Legend as in Fig. 1

and the spanwise components are strongly altered using the SSG correction. On the other hand, the SSG correction improves the model predictions in the buffer layer and thus, although the asymptotic behavior of $a_{11}$ and $a_{33}$ is altered, it offers here a better description. Finally, moving to the predicted production-to-dissipation ratio which is related to the solution for $N$ through Eq. 36, Fig. 5 shows that the peak and its location in the near wall region are correctly reproduced and that the results are almost independent of the formulation based on the elliptic blending methodology. However, both the peak and the plateau where production and dissipation are balanced are overestimated by the model.

### 4.2 Turbulent channel flow

The full model predictions are now assessed on the same fully developed channel cases at $\mathrm{Re}_\tau = 550$ and 2000. The bulk Reynolds number $\mathrm{Re}_b = U_b\delta/\nu$ from DNS data [27] corresponds respectively to 10120 and 43496. The two-dimensional mean flow is periodic in the streamwise direction and the bulk Reynolds number is imposed via an adaptive force.

Fig. 6 and 7 show that the predicted mean velocity and thus shear stress profiles are almost insensitive to the model formulation, at least with the values adopted for the coefficients $C_L$ and $A_1$ that result from model calibration for this flow case. This contrasts with the results displayed in Fig. 8 for the normal stresses that shows that the SSG-like correction significantly improves the model predictions. Otherwise, the predicted normal stresses slightly depend on the exponent used for the elliptic blending coefficient $f = \alpha^2$ or $f = \alpha^3$ but the results remain comparable. It is worth recalling here that the obtained underestimation of the streamwise normal stress in the log-layer which appears clearly at $\mathrm{Re}_\tau = 2000$, is not a consequence of the elliptic blending approach but is related to the inability of pressure-strain models to predict large scale motions in the log-layer coming from the central part of the channel [13]. Fig. 9 shows that, contrary to the a priori evaluation for which over-predictions were systematically reported, the production-to-dissipation ratio is accurately predicted by the various model formulations. Here again, the SSG-like correction seems to perform better but the results remain similar.

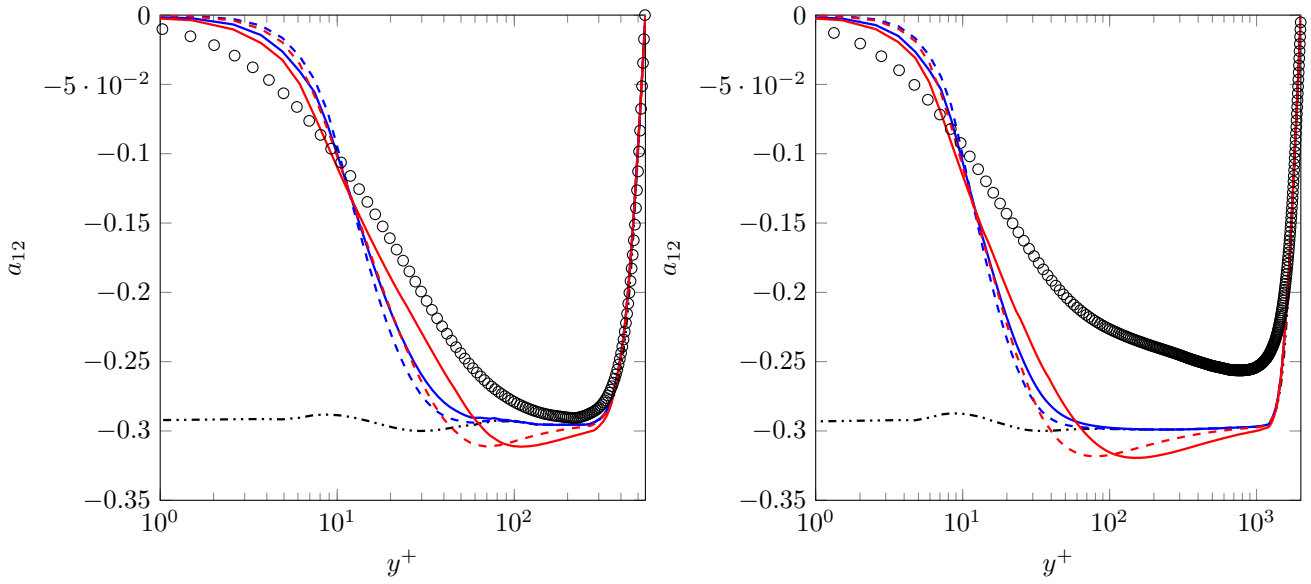


Figure 3: Turbulent channel flow. A priori test of the model for the $a_{12}$ anisotropy at $\mathrm{Re}_\tau = 550$ (left) and $\mathrm{Re}_\tau = 2000$ (right). Legend as in Fig. 1

The previous results obtained from a priori or full model evaluation show that the algebraic formulation produce good predictions in a channel flow which is a classical corner stone for wall-bounded turbulent flow model validation. While the SSG-like correction improves significantly the predictions regarding the normal components of the Reynolds stresses, the formulations $f = \alpha^2$ and $f = \alpha^3$ lead to very similar predictions. As stated in Section 2.1, the proper asymptotic behaviour corresponds to $f = \alpha^3$ and thus this choice will be adopted subsequently.

### 4.3 Channel with rib roughness

Next we consider the case of a fully developed turbulent flow in a channel with transverse rib roughness on one wall. The mean flow remains two-dimensional and a schematic of the computational domain $[0, L] \times [0, H]$ is depicted in Fig. 10. The distance between two successive obstacles is referred to as $\ell$ and $h = H/10$ is the height of each obstacle. According to the pitch-to-height ratio $\ell/h$, three roughness types can be identified, namely the so-called $d$-type, intermediate and $k$-type roughness. The $d$-type roughness refers to obstacles whose height $h$ is about the same order as the distance $\ell$ and is characterized by a flow pattern depicted by stable vortices within the gap between successive obstacles. On the contrary, $k$-type roughness is characterized by $\ell$ significantly larger than $h$, and its flow pattern is rather depicted by unstable vortices that are generated behind each obstacle and that shed into the bulk flow. The cases $\ell/h = 1$ and 9 that correspond respectively to the two aforementioned roughness types are investigated here together with the intermediate case $\ell/h = 4$. Model predictions are compared with data obtained by Cui *et al.* [28] using large-eddy simulations at $\mathrm{Re}_b = HU_b/\nu = 10000$. Prescribing periodic boundary conditions in the streamwise direction, the flow is driven by prescribing a constant mass flow rate at a rib-free cross-section, given by $Q = \rho U_b (2H)^2$. A grid size of $288 \times 124$ which is clustered near the top and bottom walls ensures $y^+ \leq 1$ for the first grid node location.

Fig. 11 shows the streamlines for the three roughness types in order to illustrate the effect of the roughness type on the flow pattern. For $d$-type roughness, vortices whose length scale is proportional

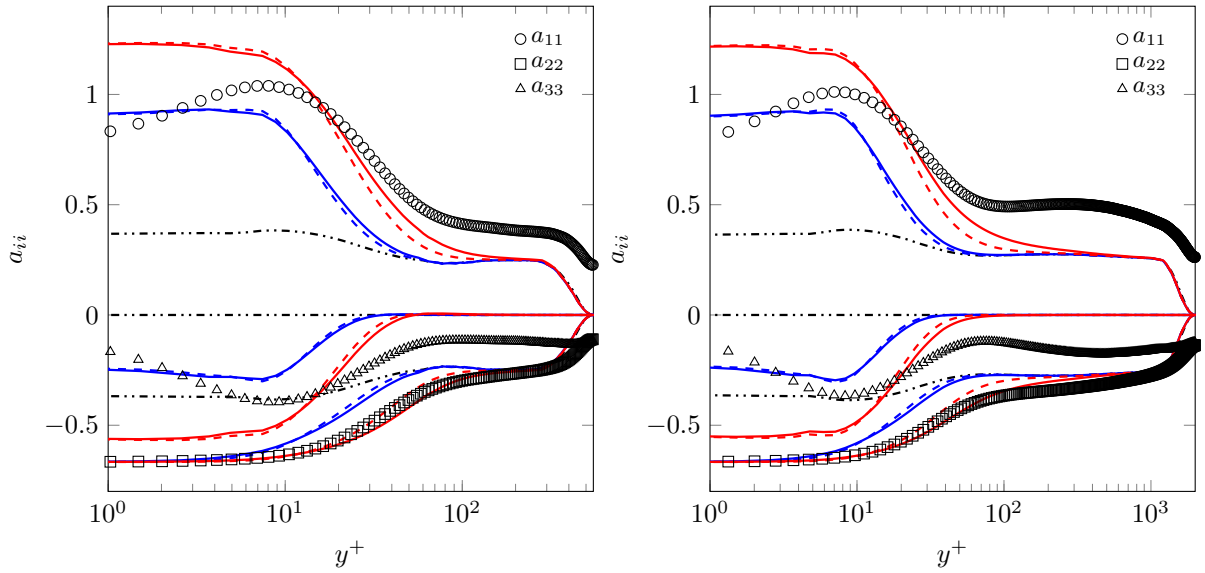


Figure 4: Turbulent channel flow. A priori test of the model for the $a_{11}$, $a_{22}$ and $a_{33}$ anisotropies at $\mathrm{Re}_\tau = 550$ (left) and $\mathrm{Re}_\tau = 2000$ (right). Legend as in Fig. 1

to $\ell$ are confined in the narrow cavities delimiting ribs without affecting the outer flow. On the other hand, for $k$-type roughness, the outer flow is altered by separation and reattachment that appear in the spacing between ribs where vortices have a length scale proportional to $k$. Finally, for intermediate roughness, vortices produced between two successive ribs have a length scale proportional to $\ell$ preventing the outer flow to be significantly affected by the ribs.

Figs. 12-13 show the streamwise mean velocity and turbulence intensity profiles along the $y$-axis at the middle of a rib and at the cavity center corresponding to the middle between two successive ribs. As usually observed for such flows, these profiles exhibit two distinct regions: a near-field region located in the vicinity of the ribs and a far-field region. The near-field region that may extend above the ribs, features mean flow profiles that are strongly related to the roughness geometry. The far-field region remains independent of the roughness geometry and closely looks like the previous channel flow case. Contrary to the previously discussed channel flow case, the analytical solution provided in Sec. 2.5.1 is no longer valid and the behavior of the iterative procedure defined by Eq. 122 to compute $N$ is assessed here according to a prescribed number of iterations. The case $n = 1$ corresponds to the first order approximation using $\Lambda(N) = 1$, the case $n = 3$ corresponds to the default case, whereas $n = 6$ is used to assess convergence. It is worth noticing that Figs. 12-13 show that the iterative sequence converges very rapidly and that the first order approximation is very close to the solution obtained at $n = 6$ for both the near-field and far-field regions.

For $d$-type roughness, Fig. 12 shows that both the predicted reversed flow within the cavity and the predicted outer flow above the ribs, that closely looks like the smooth channel flow case, agree well with reference data. The streamwise turbulence intensity displayed in Figs. 13 is also fairly well reproduced by the model. For intermediate roughness, the outer flow streamwise velocity profile at the rib and at the cavity are well reproduced while the magnitude of the reversed flow near the wall at the cavity is slightly underestimated. The streamwise turbulence intensity peak is fairly well reproduced above the rib while an underestimation seems to occur at the cavity. For $k$-type roughness, contrary to the previous cases, the mean flow features separation and reattachment and the agreement between model predictions and LES results is less satisfactory. At the cavity center, the mean flow has reattached to the cavity floor and Fig. 12 shows that the agreement between model

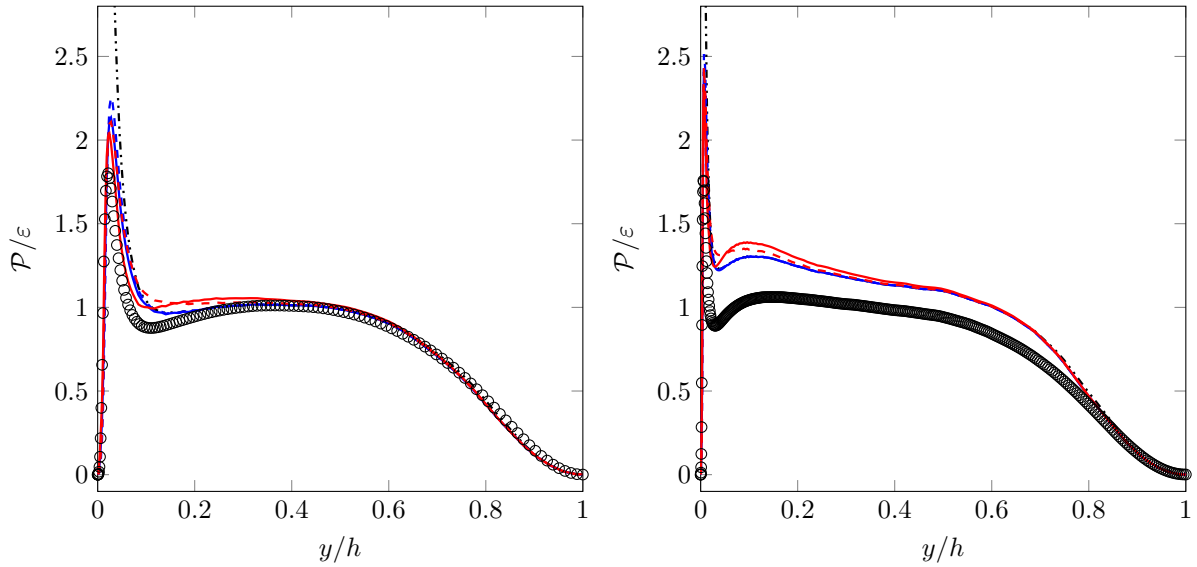


Figure 5: Turbulent channel flow. A priori test of the model for the production to dissipation ratio at $\mathrm{Re}_\tau = 550$ (left) and $\mathrm{Re}_\tau = 2000$ (right). Legend as in Fig. 1

predictions and reference data remains satisfactory. On the other hand, the mean streamwise flow above the rib that experiences an acceleration due to the reduction of the flow cross-section is not accurately predicted.

The discrepancies observed for the $k$-type roughness may originate from two distinct failures that are revealed by the distributions of the normal components of the Reynolds stresses $\overline{u'^2} + \overline{v'^2}$ and $\overline{w'^2}$ displayed in Fig. 14. The distribution of the spanwise turbulent intensity agrees fairly well with either LES [28] or DNS [29] simulation results and exhibits high values ahead of the rib owing to the blocking effect of the rib on the streamwise flow. On the other hand, contrary to reference data that report peaks at both the rib top and in the separation region behind the rib, the distribution of $\overline{u'^2} + \overline{v'^2}$ exhibits high values mainly in the upstream vicinity of the rib corner. The underestimation of turbulent energy in the separation region, as well as the overestimation of turbulent energy ahead the rib, have also been reported in [29] in the framework of the $\overline{v^2}$-$f$ modeling approach. The underestimation of turbulent kinetic energy in the separation region is related to the well-known difficulty of RANS models in dealing with vortex shedding. On the other hand, according to [29], the overestimation of turbulent kinetic energy ahead the rib is mainly related to the peak of turbulent kinetic energy production, occuring upstream the rib corner. It may be tempting to relate this behavior to the expression of the production term for eddy viscosity models and to the stagnation point anomaly [30] but the results obtained here using a second-order-like algebraic modeling of the Reynolds stresses together with the analysis provided by Colombié *et al.* [31] regarding impinging jets, suggests that such a behavior is not restricted to eddy viscosity models and requires a more elaborate second-order modeling. It is beyond the scope of this paper to provide a comprehensive discussion about the observed behavior, the analysis proposed in [31] suggests that the failure of second-order closures in predicting stagnation areas is related to the model for pressure diffusion.

### 4.4 Square duct

A three-dimensional case is now addressed. It consists in the fully developed turbulent flow in a square duct. While the streamwise direction is statistically homogeneous as the channel flow case,

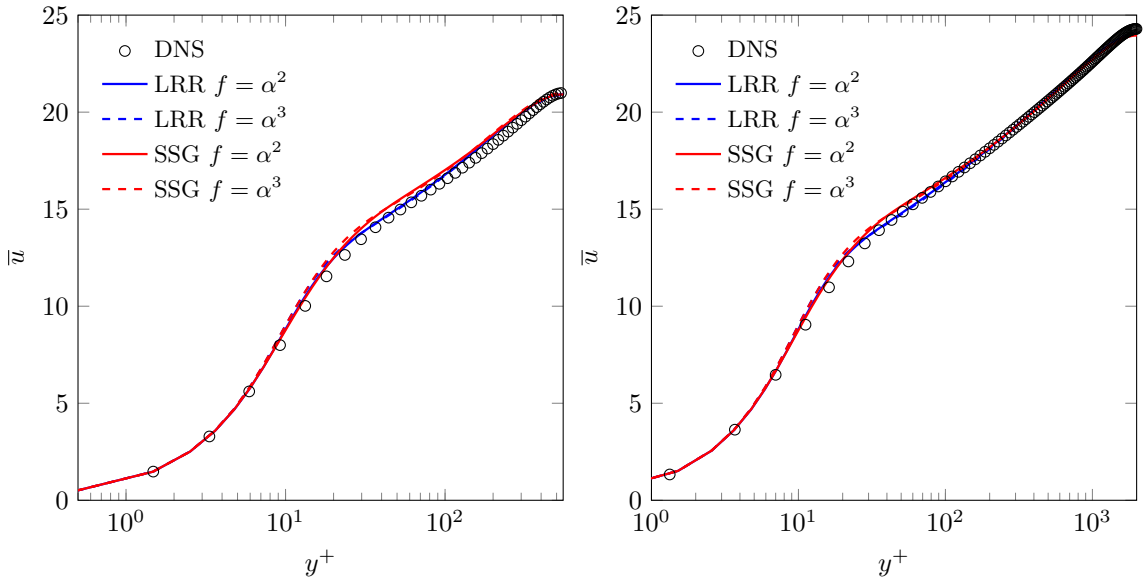


Figure 6: Turbulent channel flow. Comparison of model predictions with DNS data for the streamwise mean velocity at $\mathrm{Re}_\tau = 550$ (left) and $\mathrm{Re}_\tau = 2000$ (right)

the flow is considered as three-dimensional because contrary to the channel flow case, the square cross-section is responsible for the anisotropy between the normal components of Reynolds stresses, that leads to secondary motions in the cross-stream plane. As outlined in the introduction, while secondary motions are restricted in practice to a few percent of the streamwise bulk flow, they may have some important consequences on the distribution of either passive or active scalars and their prediction thus remains important. Linear eddy viscosity models are known to be unable to generate such secondary flows and this calls for the use of more sophisticated models. Both differential and explicit algebraic Reynolds stress models are thus natural candidates to predict normal stress anisotropy. Previous results obtained from second-moment closures at low to moderate Reynolds numbers agree fairly well with reference data. For instance, in [32], a second-moment closure using the quasi-linear SSG pressure-strain model associated with elliptic relaxation, is used. It is thus of primary interest to assess the predictive capabilities of the proposed model, based on a similar but simpler formulation.

Prescribing symmetry conditions at $y = z = h$, numerical simulations are performed on a quarter of the duct $[0; 2\pi h] \times [0; h] \times [0; h]$. The flow is sustained by prescribing a constant mass flow rate at a cross-section, given by $Q = \rho U_b h^2$. Numerical results are compared with DNS data obtained by Pirozzoli *et al.* [33] at $\mathrm{Re}_\tau = h u_\tau/\nu = 519$ and 1055, where $h$ is the duct half width. The corresponding bulk Reynolds numbers $\mathrm{Re}_b = 2hU_b/\nu$ are respectively 17800 and 40000. The results are displayed on the corner bisector $y = z$ where, due to symmetry, $\overline{v} = \overline{w}$ for the mean flow quantities while $\overline{v'^2} = \overline{w'^2}$ and $\overline{u'v'} = \overline{u'w'}$ for the turbulent quantities.

Except near the corner, the square duct geometry is very similar to the channel flow case for which an analytical solution is available for $N$, or equivalently, for the production-to-dissipation ratio. As a result, the iterative sequence, provided by Eq. 122, is expected to quickly converge here. The behavior of the iterative sequence is illustrated on Figs. 15, 16 and 17 that compare respectively the predicted mean streamwise velocity, the mean cross-wise velocity and the production-to-dissipation ratio at the two Reynolds numbers with DNS data along the corner bisector. As expected, the sequence quickly converges and the analytical two-dimensional solution that corresponds to the initial guess at $n = 1$

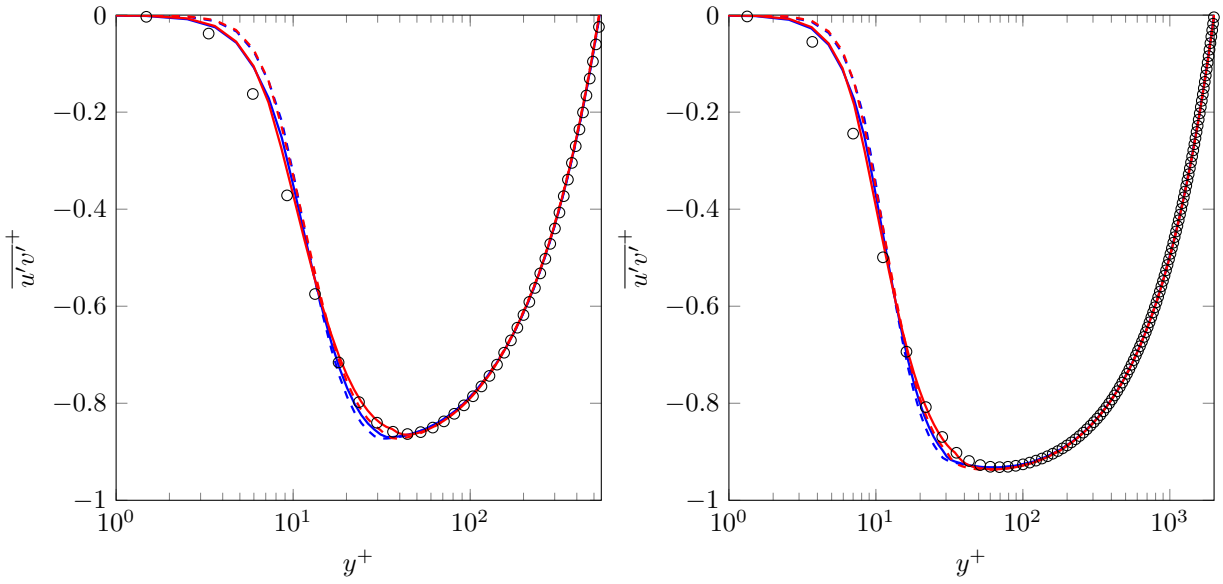


Figure 7: Turbulent channel flow. Comparison of model predictions with DNS data for the shear stress at $\mathrm{Re}_\tau = 550$ (left) and $\mathrm{Re}_\tau = 2000$ (right). Legend as in Fig. 6

is nearly identical to the solution at $n = 6$. As usually observed, the streamwise velocity shown in Fig. 15 is correctly predicted while the secondary mean flow is captured but remains underpredicted as illustrated on Fig. 16. Moving on the production-to-dissipation ratio displayed in Fig. 17, the local minimum usually observed at $y^+ \simeq 50$ [34] is reproduced but the ratio remains overpredicted in a large part of the boundary layer resulting in an overprediction of the turbulent kinetic energy level.

In order to get more detailed insights about the predicted mean streamwise flow and secondary motions, Fig. 18 shows the distribution of the dimensionless primary shear stress $\overline{u'v'}^+$, the normal stress anisotropy $\overline{v'^2}^+ - \overline{w'^2}^+$ and the secondary shear stress $\overline{v'w'}^+$ over one quadrant of the duct cross-section. The primary shear stress is involved in the mean streamwise momentum transport equation and thus affects directly the mean streamwise velocity. As expected, the results displayed in Fig. 18 confirm the good model performances regarding the mean streamwise flow and show that the predicted primary shear stress agrees well with DNS data. On the other hand, the normal stress anisotropy and the secondary shear stress are involved in the mean streamwise vorticity transport equation and thus affect the secondary motion. The results displayed in Fig. 18 show that the normal stress anisotropy is fairly well reproduced while the secondary shear stress is significantly overpredicted in most part of the duct except in the vicinity of the corner where it becomes underpredicted. The same trends were reported in [32] at a lower Reynolds number resulting in an imbalance between the turbulence source terms of the mean streamwise vorticity transport equation and leading to an underestimation of secondary motion. Hence, attributing the observed discrepancies between model predictions and DNS data to the secondary shear stress, this highlights the importance of a reliable pressure-strain model to accurately predict secondary motion.

Despite the observed discrepancies, it is worth pointing out that the model predictions outperforms most of the eddy viscosity $k$-$\varepsilon$ models [35] and seems to produce comparable predictions with either the $v^2$-$f$ model involving the linear algebraic relation from Pecnik and Iaccarino [35, 36] or the full Reynolds stress model [32]. However, the proposed model is likely to be more general in comparison with the $v^2$-$f$ model, at least from a theoretical point of view, and contains only three differential equations for $k$, $\varepsilon$ and the elliptic blending coefficient $\alpha$.

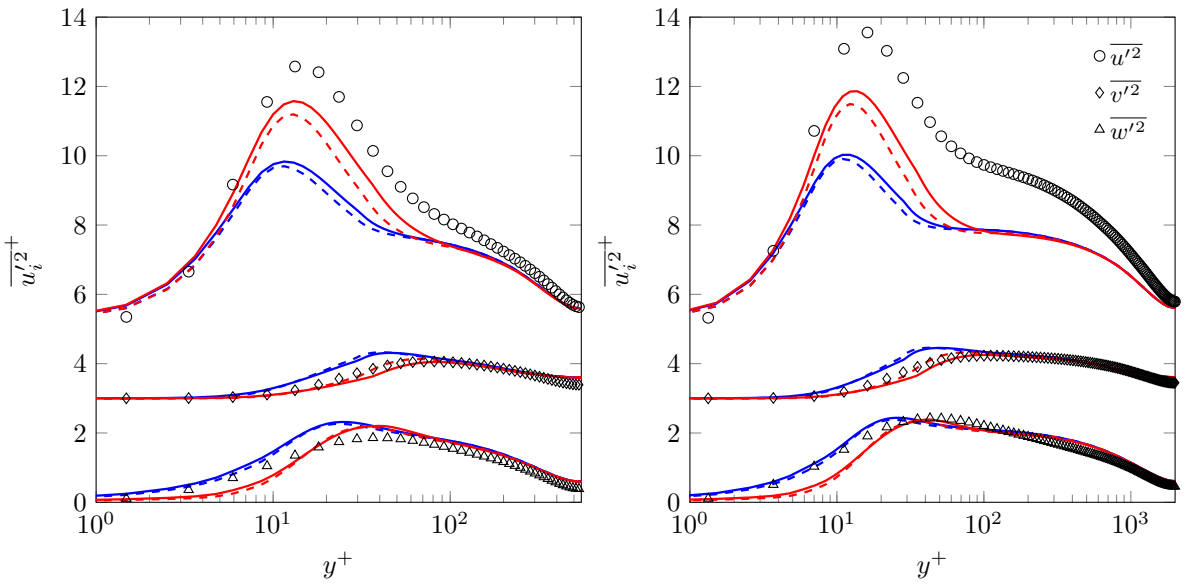


Figure 8: Turbulent channel flow. Comparison of model predictions with DNS data for the normal stresses at $\mathrm{Re}_\tau = 550$ (left) and $\mathrm{Re}_\tau = 2000$ (right). Legend as in Fig. 6. Streamwise and normalwise components are shifted for clarity.

## 5 Conclusion

The explicit algebraic stress model proposed in this work for wall-bounded turbulent flows has been obtained in the frame of the elliptic blending strategy originally proposed by Manceau and Hanjalić [5] to represent wall-induced blocking effects on Reynolds stresses. Following the standard weak equilibrium hypothesis, the model has been derived on the basis of a pressure-strain model corresponding to a blending between a linear model as adopted by Wallin and Johansson [18] far from the wall and an alternate empirical formulation for the near-wall asymptotic limit that remains close to the original version [5]. The use of a linear formulation far from the wall and a slightly modified near-wall formulation has been motivated by the requirement of reducing as much as possible the non-linearities related to the pressure-strain model. In addition, a correction for the coefficient related to the mean strain rate of the far-from-the-wall pressure-strain model mimicking the SSG model has also been assessed as it was expected to play a significant role in the near-wall region. Rather than truncating a priori the integrity basis as proposed in [14, 15] as a first tentative to derive an explicit algebraic model using the elliptic blending strategy, the algebraic relation has been obtained here following a direct solution method. The resulting algebraic relation remains formally similar to standard expressions based on a linear pressure-strain model with the addition of the tensor $\boldsymbol{M}$ related to the wall orientation. For two-dimensional mean flows, the consistency condition for the production-to-dissipation ratio leads to sixth-order equation that reduces to a fourth-order equation for a flow parallel to the wall or a two-dimensional impingement point. This is a remarkable feature as most of near-wall flows correspond or come close to these two typical situations except the situation involving flow separation. An analytical solution has been obtained by identifying the physical roots in the two limiting cases, in the vicinity and far from the wall. Then, depending on the flow situation, this solution can serve as a guess to an iterative process based on the relationship giving the production-to-dissipation ratio to obtain a self-consistent model. Using a $k$-$\varepsilon$ model as a platform model with the usual set of calibration coefficients and the standard modification of the

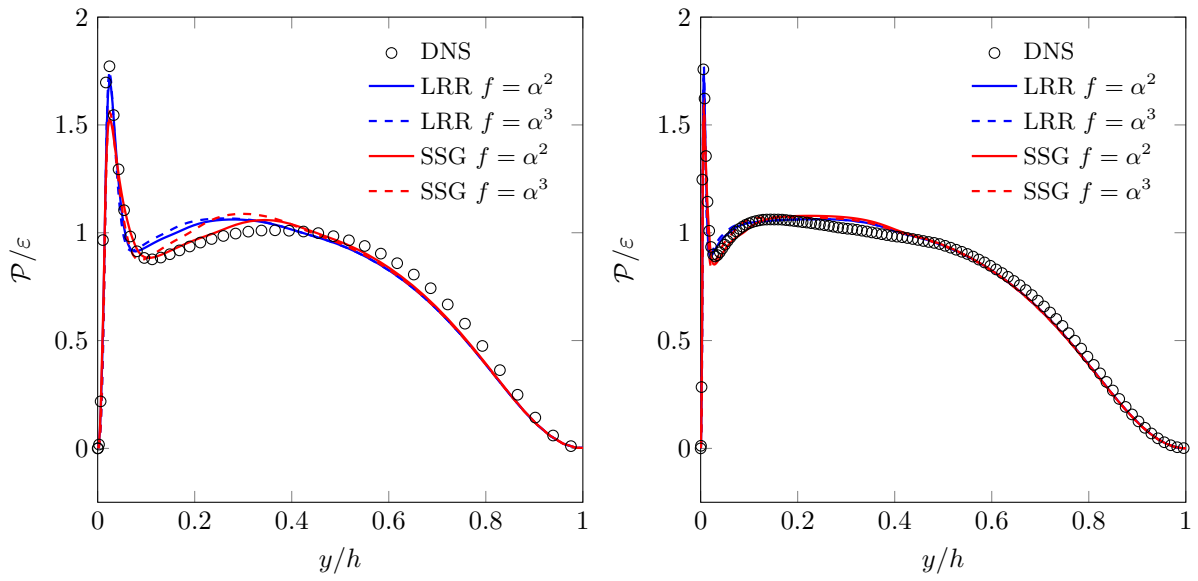


Figure 9: Turbulent channel flow. Comparison of model predictions with DNS data for the production to dissipation ratio at $\mathrm{Re}_\tau = 550$ (left) and $\mathrm{Re}_\tau = 2000$ (right)

coefficient $C_{\varepsilon 1}$ to enhance production of the dissipation in the buffer layer [8, 13], the model performances have been assessed on fully developed wall-bounded turbulent flows using the open-source solver CALIF$^3$S. The results obtained on the academic channel flow case have illustrated the very good model performances and have shown that although the asymptotic behavior of the spanwise anisotropy tensor components are altered, the SSG-like correction led to better predictions. The results obtained on the channel with rib roughness and on the square duct have confirmed the good model performances and have shown that the analytical solution for the production-to-dissipation ratio provided for two-dimensional mean flows parallel to the wall was very close to the exact solution corresponding to a self-consistent model. Finally, while this work focused on the explicit algebraic modeling in the frame of the elliptic blending strategy, some shortcomings inherited from the underlying second-order closure have also been recalled. These could call to alternate closure models to improve both algebraic and differential Reynolds stress model predictions.

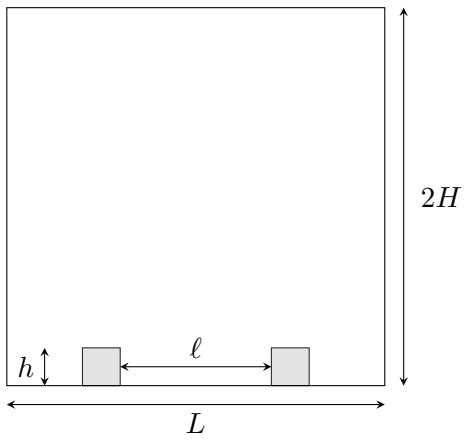


Figure 10: Schematic of a channel flow with transverse ribs on the bottom wall

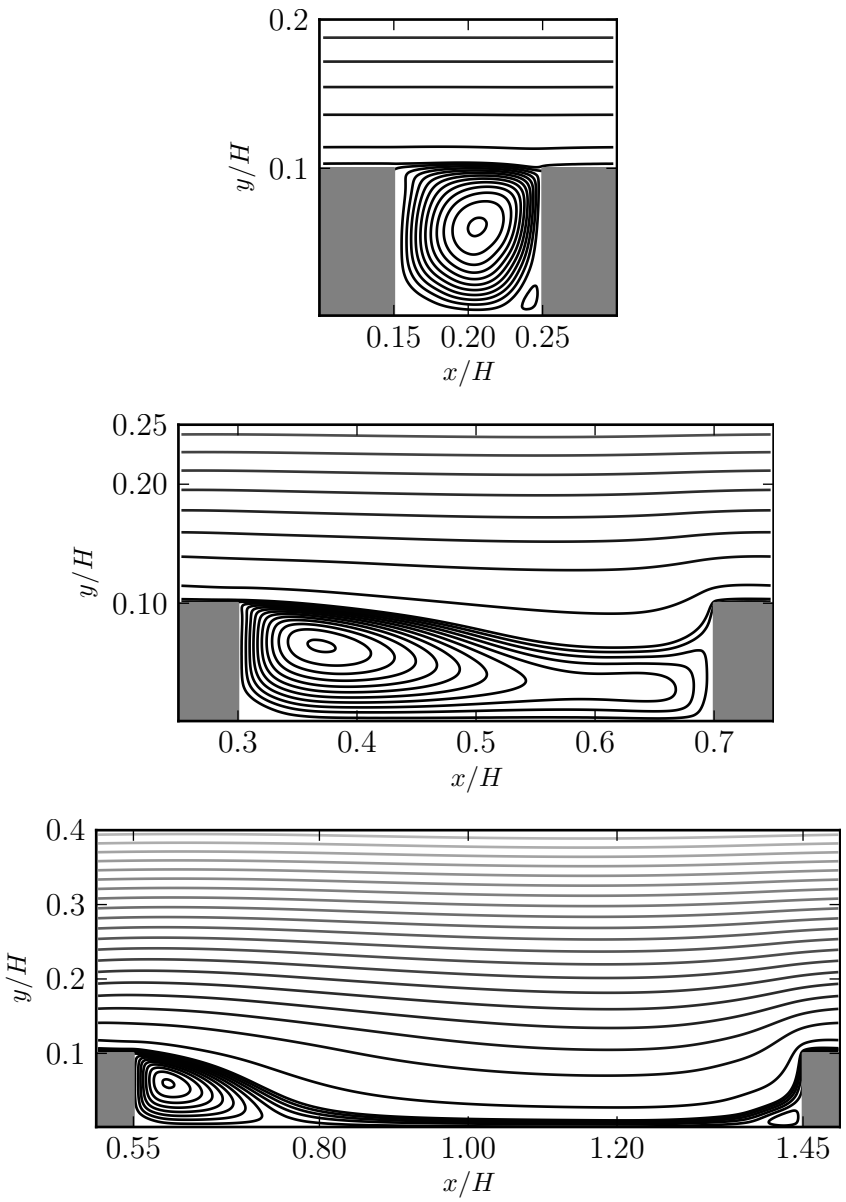


Figure 11: Channel with rib roughness. Streamlines for $d$-type (top left), intermediate (top right) and $k$-type (bottom) roughness

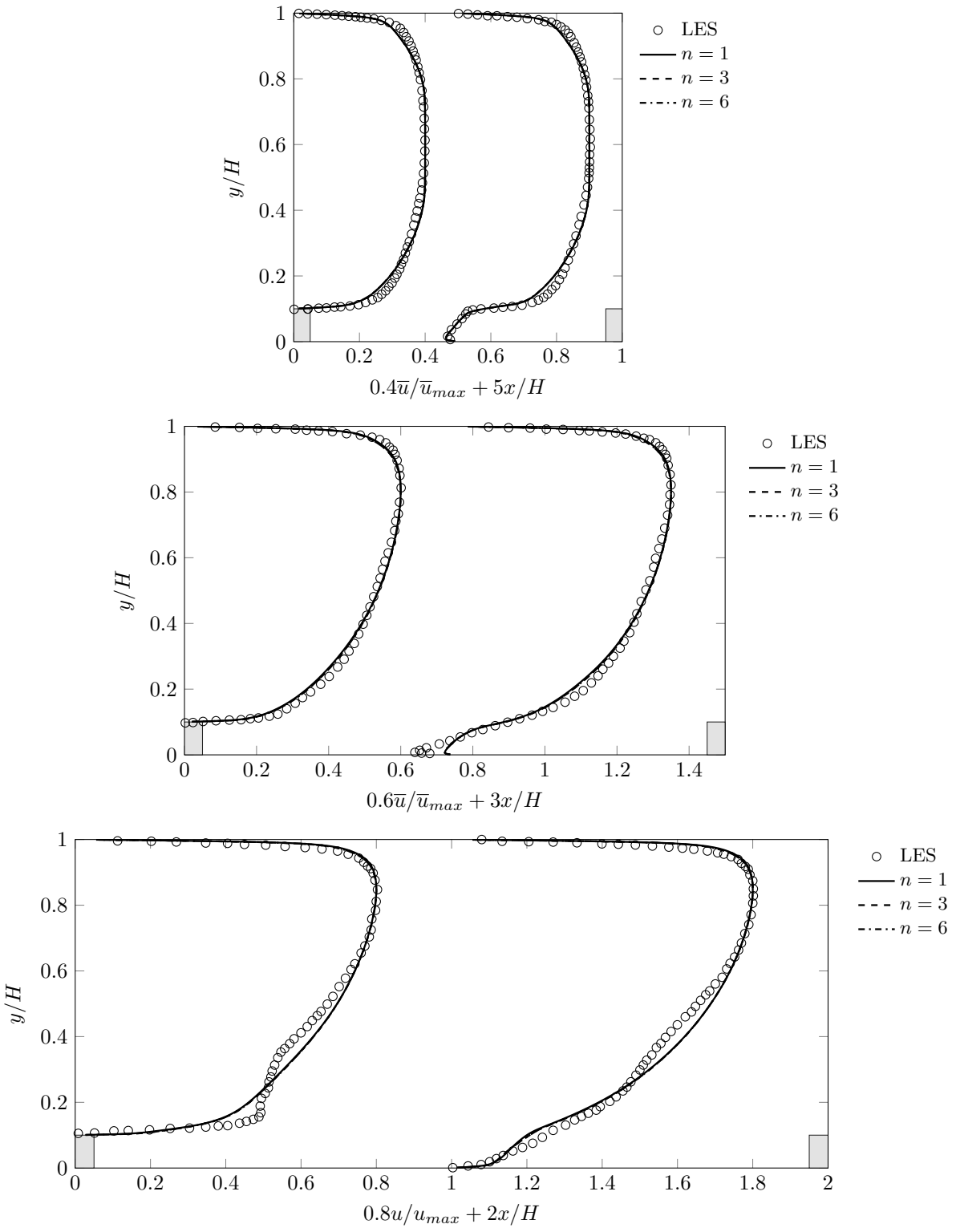


Figure 12: Channel with rib roughness. Mean streamwise velocity profiles at rib and cavity centers for $d$-type (top left), intermediate (top right) and $k$-type (bottom) roughness.

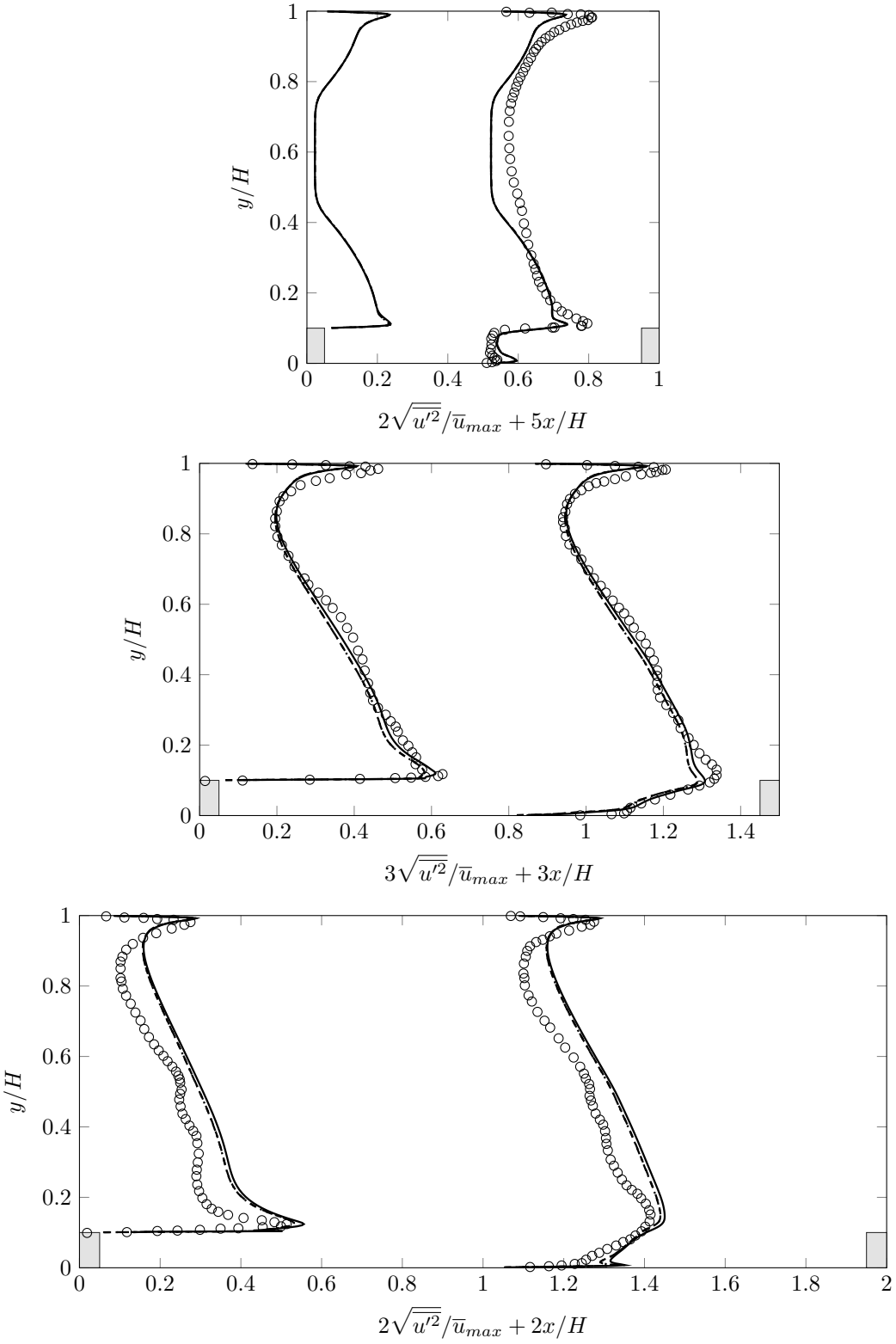


Figure 13: Channel with rib roughness. Mean streamwise turbulence intensity profiles at rib and cavity centers for $d$-type (top left), intermediate (top right) and $k$-type (bottom) roughness. Same legend as Fig. 12.

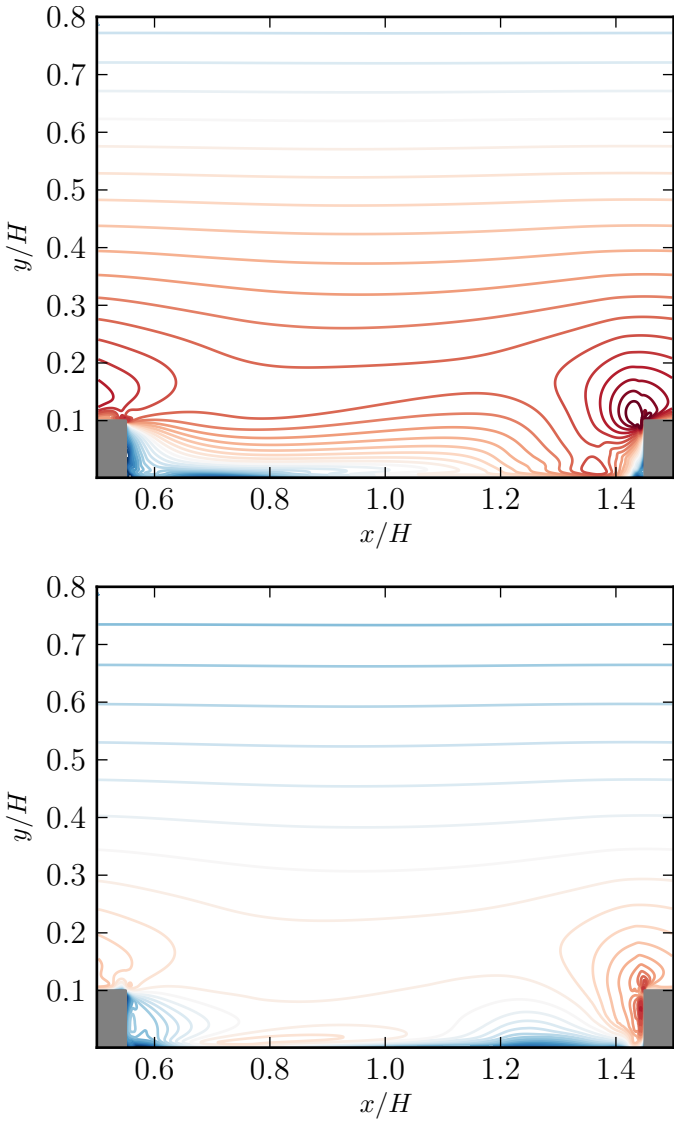


Figure 14: Channel with rib roughness, $k$-type. Turbulent intensities $\sqrt{\overline{u'^2} + \overline{v'^2}}$ (top) and $\sqrt{\overline{w'^2}}$ (bottom) normalized by the bulk velocity. Contour levels range between 0.015 (blue) and 0.45 (red)

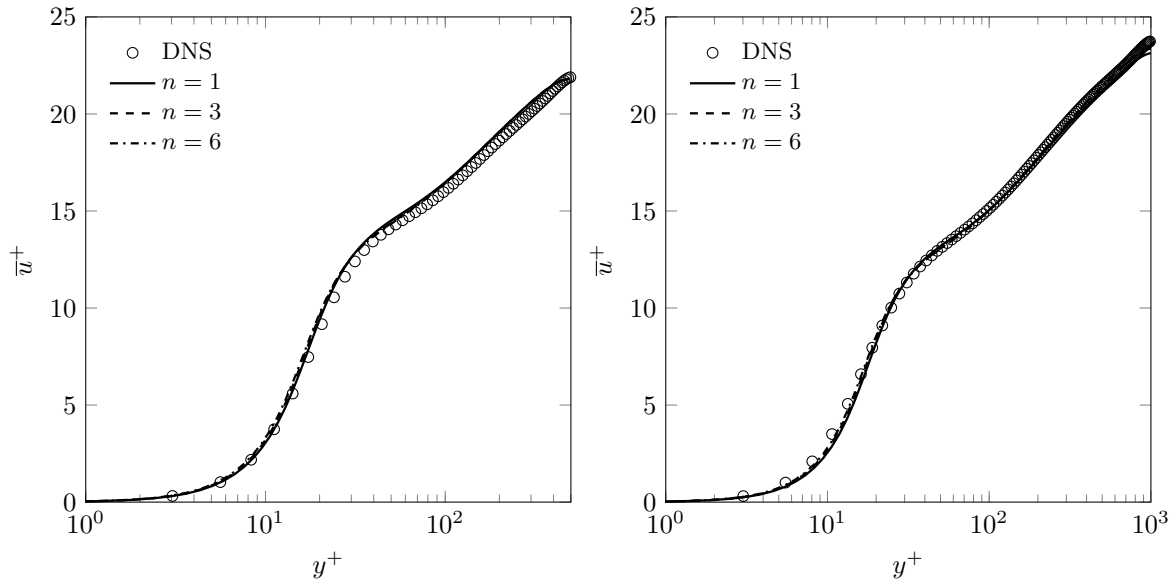


Figure 15: Square duct flow. Mean streamwise velocity along the corner bisector at $\mathrm{Re}_\tau = 500$ (left) and $\mathrm{Re}_\tau = 1000$ (right)

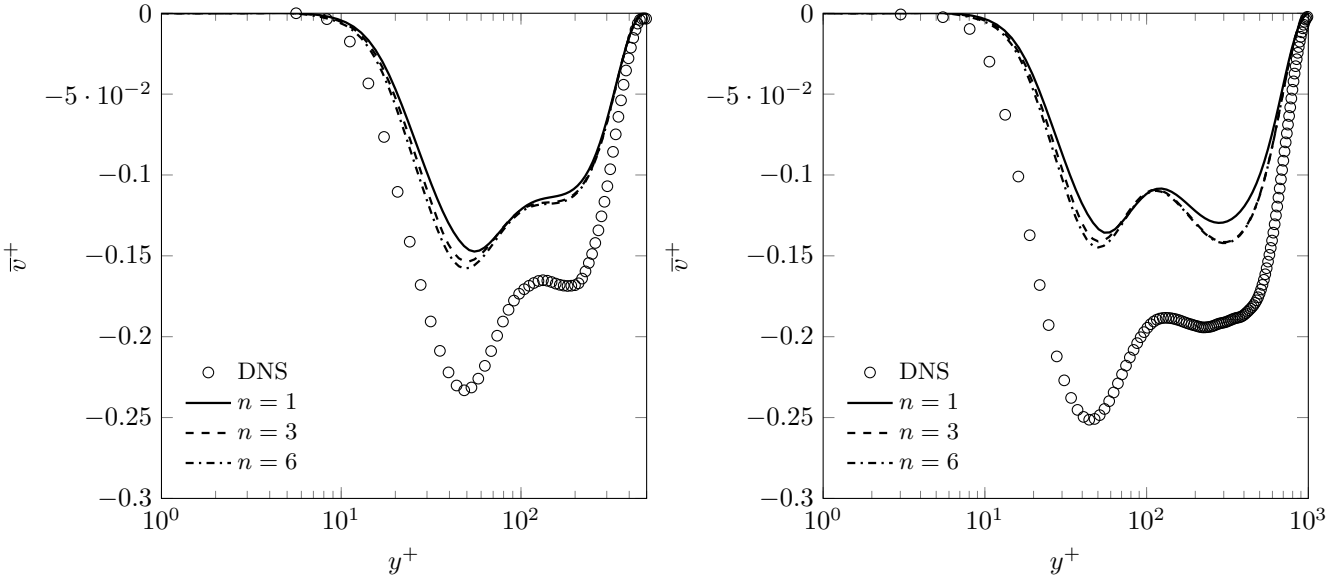


Figure 16: Square duct flow. Mean cross-wise velocity along the corner bisector at $\mathrm{Re}_\tau = 500$ (left) and $\mathrm{Re}_\tau = 1000$ (right)

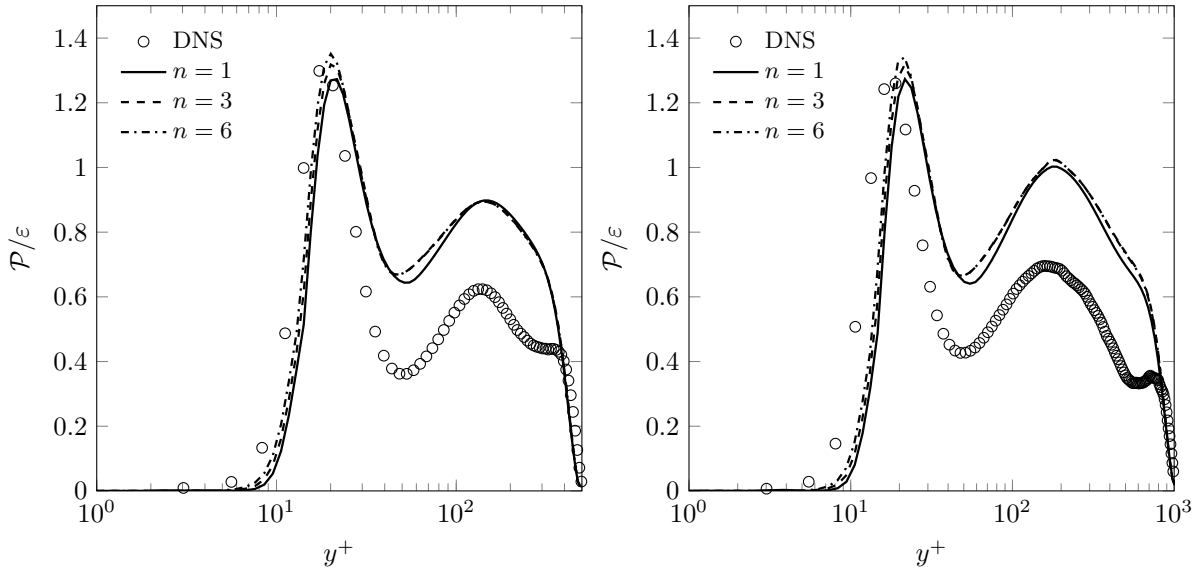


Figure 17: Square duct flow. Production-to-dissipation ratio along the corner bisector at $\mathrm{Re}_\tau = 500$ (left) and $\mathrm{Re}_\tau = 1000$ (right)

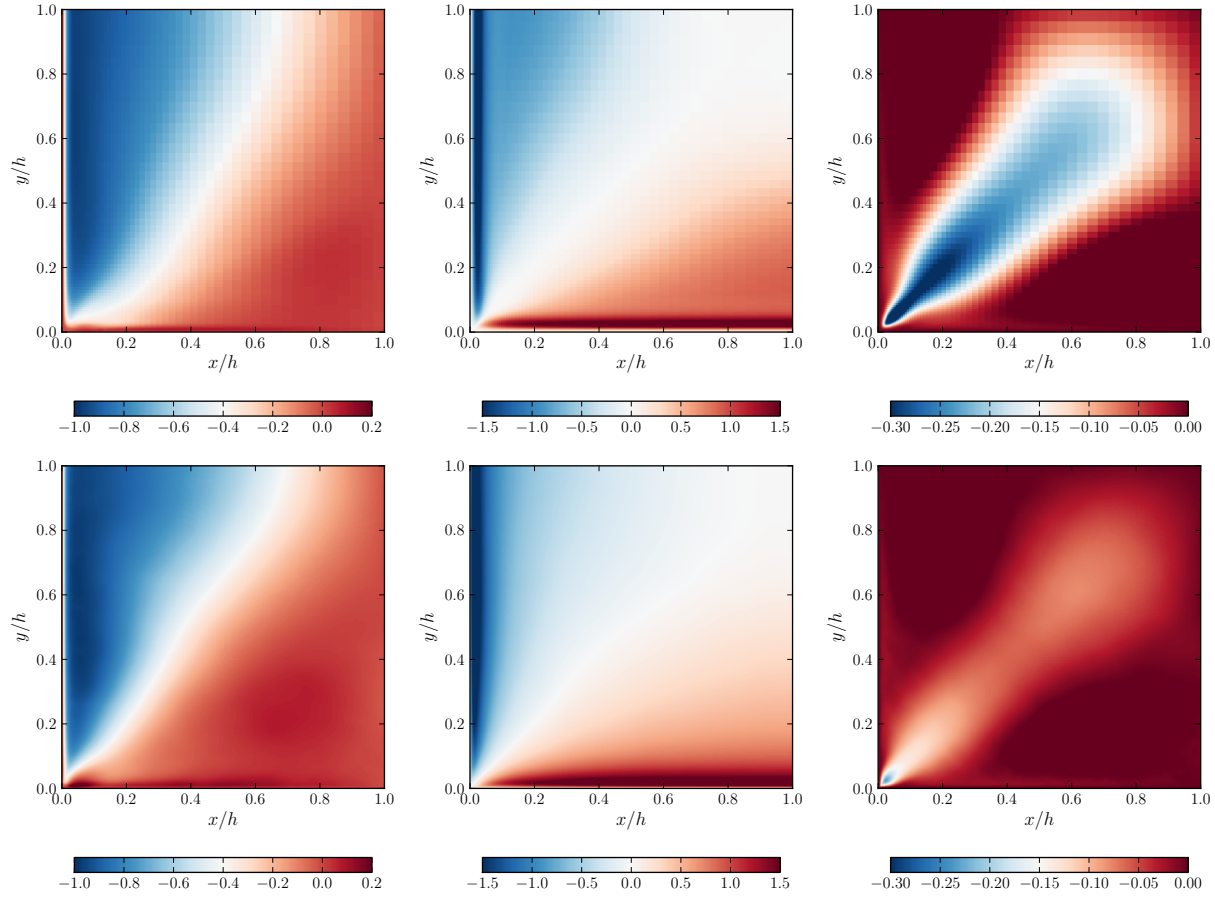


Figure 18: Square duct flow. Primary shear stress $\overline{u'v'}^+$ (left), normal stress anisotropy $\overline{v'^2}^+ - \overline{w'^2}^+$ (middle) and secondary shear stress $\overline{v'w'}^+$ (right) from model predictions (top) and DNS (bottom) at $\mathrm{Re}_\tau = 1000$

# A Cayley-Hamilton theorem derived relationships

## A.1 Two-dimensional case

In the two-dimensional case, the statement of the Cayley-Hamilton theorem for an arbitrary tensor $a$ reads :

$$a^2 = tr\{a\}a - det(a)I \tag{128}$$

where $I$ is the two-dimensional unit tensor and $tr\{\cdot\}$ refers to the trace operator. Taking the trace of the above relation leads to the following expression for $det(a)$ :

$$det(a) = \frac{1}{2}\left[(tr\{a\})^2 - tr\{a^2\}\right] \tag{129}$$

Important simplifications arise of the tensor $a$ is traceless. By introducing $II_a = tr\{a^2\}$, Eq. 128 reduces in this case to:

$$a^2 = \frac{1}{2}II_a I \tag{130}$$

On the other hand, we note that for two arbitrary two-dimensional tensors $b$ and $c$, one has:

$$(b+c)^2 = b^2 + c^2 + bc + cb$$
$$tr\{(b+c)^2\} = tr\{b^2\} + tr\{c^2\} + 2tr\{bc\}$$

Hence, using the Cayley-Hamilton theorem Eq. 130 with $a = b+c$, collecting the results and equating the equal powers of $b$ and $c$ we get:

$$bc + cb = tr\{bc\}I \tag{131}$$

Finally, post multiplying Eq. 131 by $b$ and using again the Cayley-Hamilton theorem Eq. 130 for $b$ leads to:

$$bcb = tr\{bc\}b - \frac{1}{2}tr\{b^2\}c \tag{132}$$

## A.2 Three-dimensional case

In the three-dimensional case, the statement of the Cayley-Hamilton theorem for an arbitrary tensor $a$ reads:

$$a^3 = tr\{a\}a^2 - \frac{1}{2}\left[tr\{a\}^2 - tr\{a^2\}\right]a + det(a)I \tag{133}$$

where $I$ is the three-dimensional unit tensor and $tr\{\cdot\}$ refers to the trace operator. Taking the trace of the above relation leads to the following expression for $det(a)$:

$$det(a) = \frac{1}{6}\left[2tr\{a^3\} + tr\{a\}^3 - 3tr\{a\}tr\{a^2\}\right] \tag{134}$$

Important simplifications arise for an arbitrary traceless tensor, Eq. 133 reduces in this case to:

$$a^3 = \frac{1}{2}II_a a + \frac{1}{3}III_a I \tag{135}$$

On the other hand, we note that for arbitrary three-dimensional symmetric tensor $s$ and arbitrary three-dimensional antisymmetric tensor $o$, one has:

$$\begin{aligned}(s+o)^2 &= s^2 + so + os + o^2 \\ tr\{(s+o)^2\} &= II_s + II_o \\ (s+o)^3 &= s^3 + (s^2o + sos + os^2) + (so^2 + oso + o^2s) + o^3 \\ tr\{(s+o)^3\} &= III_s + 3III_{so^2}\end{aligned}$$

Hence, using the Cayley-Hamilton theorem Eq. 135 with $a = s+o$, collecting the results and equating the equal powers of $s$ and $o$ we get:

$$s^3 = \frac{1}{2}II_s s + \frac{1}{3}III_s I \tag{136}$$

$$s^2o + sos + os^2 = \frac{1}{2}II_s o \tag{137}$$

$$so^2 + oso + o^2s = \frac{1}{2}II_o s + III_{so^2} I \tag{138}$$

$$o^3 = \frac{1}{2}II_o o \tag{139}$$

Hence, it follows the above usefull additional relations:

$$sos^2 + s^2os = -\frac{1}{3}III_s o \tag{140}$$

$$s^2os^2 = -\frac{1}{4}II_s^2 o - \frac{1}{3}III_s(os + so) + \frac{1}{2}II_s(os^2 + s^2o) \tag{141}$$

$$o^2so^2 = -\frac{1}{4}II_o^2 s + \frac{1}{2}II_o(so^2 + o^2s) + III_{so^2}o^2 - \frac{1}{2}II_o III_{so^2} \tag{142}$$

In the same way, using again the Cayley-Hamilton theorem Eq. 135 but with $a = s+b$ where both $s$ and $b$ are symmetric tensors, collecting the results and equating the equal powers of $s$ and $b$ we get the following relations:

$$s^2b + sbs + bs^2 = \frac{1}{2}II_s b + II_{sb}s + III_{bs^2} I \tag{143}$$

$$sb^2 + bsb + b^2s = \frac{1}{2}II_b s + II_{sb}b + III_{sb^2} I \tag{144}$$

Hence, it follows the above usefull additional relations:

$$bsb^2 + b^2sb = II_{sb}b^2 + III_{sb^2}b - \frac{1}{3}III_b s \tag{145}$$

$$\begin{aligned}b^2sb^2 = &-\frac{1}{4}II_b^2 s + III_{sb^2}b^2 - \frac{1}{3}III_b(bs + sb) \\ &+ \frac{1}{2}II_b(sb^2 + b^2s) + \left(\frac{1}{3}II_{sb}III_b - \frac{1}{2}II_b III_{sb^2}\right)\end{aligned} \tag{146}$$

# B Solution of the approximate quartic equation

Following a similar analysis provided by Grigoriev *et al.* [37], the four roots of Eq. 112 are given by

$$\tilde{N} = \frac{1}{4} + \frac{1}{2}R_{1,2} \pm \frac{1}{2}\sqrt{\frac{1}{2} + a - z + R_{1,2} + \frac{2b-z}{R_{1,2}}}\,, \quad R_{1,2} = \pm\sqrt{\frac{1}{4} + a + z} \tag{147}$$

where $z$ is a real root of the resolvent equation $z^3 + az^2 + (b+4c)z - (b^2 - c - 4ac) = 0$. Introducing the change of variable $z = (b^2 - c - 4ac)\hat{N}^{-1}/(b+4c)$, the resolvent cubic equation reads:

$$\hat{N}^3 - \hat{N}^2 - A\hat{N} - B = 0\,, \quad A = \frac{a(b^2 - c - 4ac)}{(b+4c)^2}\,, \quad B = \frac{(b^2 - c - 4ac)^2}{(b+4c)^3} \tag{148}$$

The interest in introducing this change of variable is related to the case $c = 0$ that leads to $A = a$ and $B = b$. This case is of particular interest since it corresponds to far from the wall regions in which the elliptic blending model reduces to the homogeneous one with:

$$a = \left(\frac{27}{10} II_S + 2II_\Omega\right) {c_1'}^{-2}\,, \quad b = -2II_\Omega {c_1'}^{-2} \tag{149}$$

In the case $c = 0$, Eq. 148 for $\hat{N}$ is identical to Eq. 112 for $\tilde{N}$, except the trivial root $\tilde{N} = 0$, and the physical root corresponds to the positive root already obtained for the homogeneous part [38, 18]:

$$\hat{N} = \begin{cases} \dfrac{1}{3} + \left(P_1 + \sqrt{P_2}\right)^{1/3} + \text{sign}\left(P_1 - \sqrt{P_2}\right)|P_1 - \sqrt{P_2}|^{1/3} & P_2 \geq 0 \\ \dfrac{1}{3} + 2\sqrt{P}\cos\left(\dfrac{1}{3}\arccos\left(\dfrac{P_1}{P^{3/2}}\right)\right) & P_2 < 0 \end{cases} \tag{150}$$

with

$$P_2 = P_1^2 - P^3\,, \quad P = \frac{1+3A}{9}\,, \quad P_1 = \frac{1}{27}\left(1 + \frac{9}{2}A + \frac{27}{2}B\right) \tag{151}$$

The above physical root for $\hat{N}$ can then help to select the physical root of Eq. 147 for $\tilde{N}$. In the case $c = 0$, the change of variable reads $z = b\hat{N}^{-1}$ and, provided that $\hat{N} \geq 1$ from Eqs. 149-151, one has:

$$R_{1,2} = \pm\frac{|z - 2b|}{2|z|} = \pm\frac{1}{2}|1 - 2\hat{N}| = \pm\left(\hat{N} - \frac{1}{2}\right) \tag{152}$$

On the other hand, from the cubic equation Eq. 148, the case $c = 0$ allows to express $a$ as:

$$a = \hat{N}^2 - \hat{N} - \frac{b}{\hat{N}} \tag{153}$$

As a result, the four root given by Eq. 147 are given in the case $c = 0$ by:

$$\tilde{N} = \frac{1}{4} \pm \left(\frac{\hat{N}}{2} - \frac{1}{4}\right) \pm \frac{1}{2}\sqrt{\frac{1}{2} + \hat{N}^2 - \hat{N} - \frac{2b}{\hat{N}} \pm \left(\hat{N} - \frac{1}{2} + \frac{2b}{\hat{N}}\right)} \tag{154}$$

Hence, requiring that $\tilde{N} = \hat{N}$ allows to select the physical root of Eq. 147 in the homogeneous region:

$$\tilde{N} = \frac{1}{4} + \frac{1}{2}R + \frac{1}{2}\sqrt{\frac{1}{2} + a - z + R + \frac{2b - z}{R}}\,, \quad R = R_1 = \sqrt{\frac{1}{4} + a + z} \tag{155}$$

It is worth pointing out that the case $c = 0$ is no longer restricted to the homogeneous region. In the vicinity of the wall, the elliptic blending coefficient $\alpha$ tends to 0 and, for two-dimensional mean flows parallel to the wall, the equation for $N$ also reduces to a cubic equation with coefficients:

$$a = -\frac{5}{4}a_3 {c_2'}^{-2} = -\frac{3}{25}\,, \quad b = -\frac{5}{4}a_3^2 {c_2'}^{-3} = -\frac{9}{125} \tag{156}$$

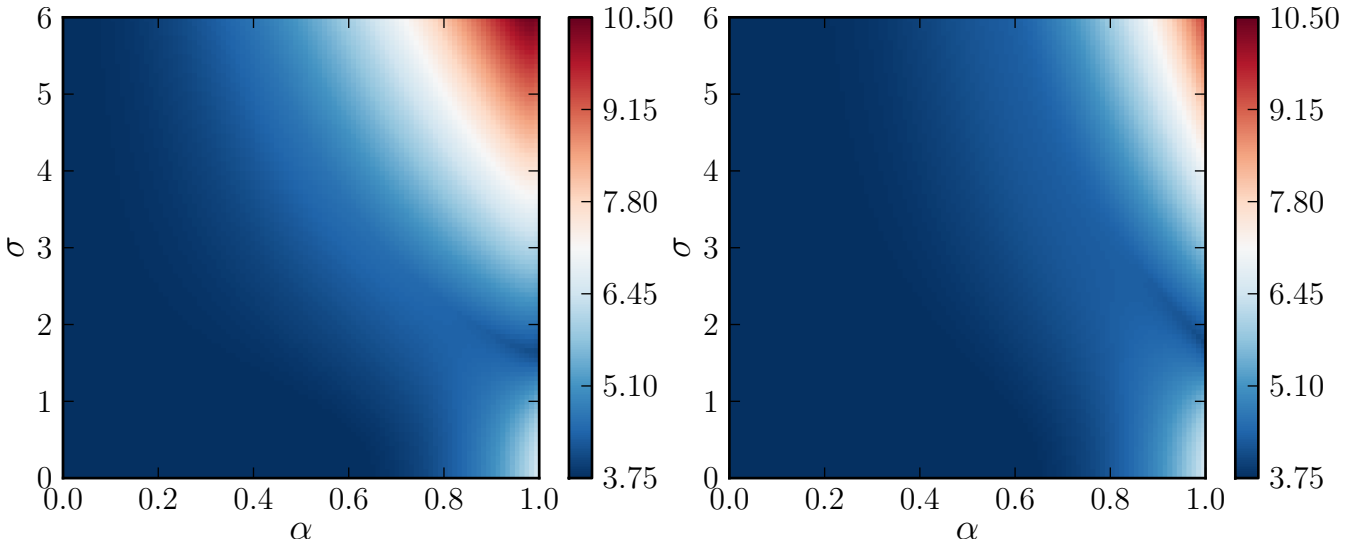


Figure 19: Physical root versus strain rate and elliptic blending coefficient for parallel shear flows with (left) or without (right) SSG-like correction

In this case, $P_2 = 0$ and $\hat{N} = -1/5$. As $c_2' > 0$, requiring that $\tilde{N} = \hat{N}$ would lead to a negative root for $\tilde{N}$. From Eq. 104, this would result further in a non vanishing kinetic energy production in the vicinity of the wall and thus, following the same reasoning as followed by Girimaji [38], this would result in a nonphysical root. On the other hand, using the root provided by Eq. 155, one obtains:

$$N = \frac{c_2'}{2}\left(1 - \hat{N}\right) + \frac{c_2'}{2}\sqrt{1 - 2\hat{N} + \hat{N}^2 - \frac{4b}{\hat{N}}} = \frac{15}{4} \tag{157}$$

In this case, the root remains positive and leads as expected to a vanishing kinetic energy production in the vicinity of the wall. On the basis on the same reasoning arguments as proposed in [37], it is tempting to assume a continuous dependence of $\tilde{N}$ on the coefficients $a$, $b$ and $c$ and to assume that the physical root in the general case $c \neq 0$ is expected to remain the same. Unfortunately, it can be shown that this may produce complex roots as the argument of the square root in the third term of the right hand side of Eq. 155 may become negative in some situations. In this case, in order avoid complex roots, the solution $\tilde{N}$ is still assumed to be given by Eq. 155 but with $R = R_2$. The behavior of the selected physical root illustrated in Figure 19 for parallel shear flows clearly confirms a continuous variation. This has further been checked for the test cases investigated in this paper for which the calculations have proven to be robust without encountering any discontinuity or complex root. Hence, even though there is a lack of available physical evidence to select the proposed root, the analysis provided in this section seems to lead to the expected physical root.

## References

[1] Y. Wang, M. Fairweather, L. F. Mortimer, Y. Zhao, and J. Yao, "Mechanisms of particle preferential concentration induced by secondary motions in a dilute turbulent square duct flow," *Physics of Fluids*, vol. 32, no. 12, p. 123313, 2020.

[2] H. Fernando, D. Zajic, S. Di Sabatino, R. Dimitrova, B. Hedquist, and A. Dallman, "Flow, turbulence, and pollutant dispersion in urban atmospheres," *Physics of Fluids*, vol. 22, no. 5, p. 051301, 2010.

[3] P. Laguionie, O. Connan, T. Tien, S. Vecchiola, J. Chardeur, O. Cazimajou, L. Solier, P. Charvolin-Volta, L. Chen, I. Korsakissok, M. Le Guellec, L. Soulhac, A. Tripathi, and D. Maro, "Investigation of a Gaussian plume in the vicinity of an urban cyclotron using helium as a tracer gas," *Atmosphere*, vol. 13, no. 8, p. 1223, 2022.

[4] V. C. Patel, W. Rodi, and G. Scheuerer, "Turbulence models for near-wall and low Reynolds number flows-a review," *AIAA journal*, vol. 23, no. 9, pp. 1308–1319, 1985.

[5] R. Manceau and K. Hanjalić, "Elliptic blending model: A new near-wall Reynolds-stress turbulence closure," *Physics of Fluids*, vol. 14, no. 2, pp. 744–754, 2002.

[6] T. Craft and B. Launder, "A Reynolds stress closure designed for complex geometries," *International Journal of Heat and Fluid Flow*, vol. 17, no. 3, pp. 245–254, 1996.

[7] P. Durbin, "Near-wall turbulent closure modeling without "damping functions"," *Theoretical and Computational Fluid Dynamics*, vol. 3, pp. 1–13, 1991.

[8] P. Durbin, "A Reynolds stress model for near-wall turbulence," *Journal of Fluid Mechanics*, vol. 249, pp. 465–498, 1993.

[9] T. Sjögren and A. Johansson, "Development and calibration of algebraic nonlinear models for terms in the Reynolds stress transport equations," *Physics of Fluids*, vol. 12, no. 6, pp. 1554–1572, 2000.

[10] K. Hanjalić, M. Popovac, and M. Hadžiabdić, "A robust near-wall elliptic-relaxation eddy-viscosity turbulence model for CFD," *International Journal of Heat and Fluid Flow*, vol. 25, no. 6, pp. 1047–1051, 2004.

[11] F. Billard and D. Laurence, "A robust $k$-$\varepsilon$- $\overline{v^2}/k$ elliptic blending turbulence model applied to near-wall, separated and buoyant flows," *International Journal of Heat and Fluid Flow*, vol. 33, no. 1, pp. 45–58, 2012.

[12] R. Manceau and K. Hanjalić, "A new form of the elliptic relaxation equation to account for wall effects in RANS modeling," *Physics of Fluids*, vol. 12, no. 9, pp. 2345–2351, 2000.

[13] R. Manceau, "Recent progress in the development of the Elliptic Blending Reynolds-stress model," *International Journal of Heat and Fluid Flow*, p. 32, 2015.

[14] R. Manceau, "Accounting for wall-induced Reynolds stress anisotropy in explicit algebraic stress models," in *Third Symposium on Turbulence and Shear Flow Phenomena*, Begel House Inc., 2003.

[15] A. G. Oceni, R. Manceau, and T. B. Gatski, "Introduction of wall effects into explicit algebraic stress models through elliptic blending," in *Progress in Wall Turbulence: Understanding and Modeling*, pp. 287–297, Springer, 2011.

[16] J. Rotta, "Statistische theorie nichthomogener turbulenz," *Zeitschrift für Physik*, vol. 129, no. 6, pp. 547–572, 1951.

[17] B. Launder, G. Reece, and W. Rodi, "Progress in the development of a Reynolds-stress turbulence closure," *Journal of Fluid Mechanics*, vol. 68, pp. 537–566, 4 1975.

[18] S. Wallin and A. Johansson, "An explicit algebraic Reynolds stress model for incompressible and compressible turbulent flows," *Journal of fluid mechanics*, vol. 403, pp. 89–132, 2000.

[19] C. Speziale, S. Sarkar, and T. Gatski, "Modelling the pressure-strain correlation of turbulence: an invariant dynamical systems approach," *Journal of fluid mechanics*, vol. 227, pp. 245–272, 1991.

[20] I. Grigoriev and W. Lazeroms, "Direct solution for the anisotropy tensor in explicit algebraic Reynolds stress models," 2016. Methodological note.

[21] W. Lazeroms, G. Brethouwer, S. Wallin, and A. Johansson, "Efficient treatment of the nonlinear features in algebraic Reynolds-stress and heat-flux models for stratified and convective flows," *International Journal of Heat and Fluid Flow*, vol. 53, pp. 15–28, 2015.

[22] T. Jongen and T. Gatski, "General explicit algebraic stress relations and best approximation for three-dimensional flows," *International Journal of Engineering Science*, vol. 36, no. 7-8, pp. 739–763, 1998.

[23] A. Hellsten and S. Wallin, "Explicit algebraic Reynolds stress and non-linear eddy-viscosity models," *International Journal of Computational Fluid Dynamics*, vol. 23, no. 4, pp. 349–361, 2009.

[24] D. Wilcox, "Formulation of the $k$-$\omega$ turbulence model revisited," *AIAA journal*, vol. 46, no. 11, pp. 2823–2838, 2008.

[25] S. Lardeau and R. Manceau, "Computations of complex flow configurations using a modified elliptic-blending Reynolds-stress model," in *10th International ERCOFTAC Symposium on Engineering Turbulence Modelling and Measurements*, p. unknown, 2014.

[26] F. Boyer, F. Dardalhon, C. Lapuerta, and J.-C. Latché, "Stability of a Crank-Nicolson pressure correction scheme based on staggered discretizations," *International Journal for Numerical Methods in Fluids*, vol. 74, no. 1, pp. 34–58, 2014.

[27] S. Hoyas and J. Jiménez, "Reynolds number effects on the Reynolds-stress budgets in turbulent channels," *Physics of Fluids*, vol. 20, no. 10, p. 101511, 2008.

[28] J. Cui, V. Patel, and C.-L. Lin, "Large-eddy simulation of turbulent flow in a channel with rib roughness," *International Journal of Heat and Fluid Flow*, vol. 24, no. 3, pp. 372–388, 2003.

[29] T. Ikeda and P. Durbin, "Direct simulations of a rough-wall channel flow," *Journal of Fluid Mechanics*, vol. 571, pp. 235–263, 2007.

[30] P. Durbin, "On the $k$-$\varepsilon$ stagnation point anomaly," *International Journal of Heat and Fluid Flow*, vol. 17, pp. 9–90, 1996.

[31] A. Colombié, E. Laroche, F. Chedevergne, R. Manceau, F. Duchaine, and L. Gicquel, "Large-eddy-simulation-based analysis of Reynolds-stress budgets for a round impinging jet," *Physics of Fluids*, vol. 33, no. 11, p. 115109, 2021.

[32] P. Reif and H. Andersson, "Prediction of turbulence-generated secondary mean flow in a square duct," *Flow, Turbulence and Combustion*, vol. 68, no. 1, pp. 41–61, 2002.

[33] S. Pirozzoli, D. Modesti, P. Orlandi, and F. Grasso, "Turbulence and secondary motions in square duct flow," *Journal of Fluid Mechanics*, vol. 840, pp. 631–655, 2018.

[34] G. Mompean, S. Gavrilakis, L. Machiels, and M. Deville, "On predicting the turbulence-induced secondary flows using nonlinear $k$-$\varepsilon$ models," *Physics of Fluids*, vol. 8, no. 7, pp. 1856–1868, 1996.

[35] D. Modesti, "A priori tests of eddy viscosity models in square duct flow," *Theoretical and Computational Fluid Dynamics*, vol. 34, no. 5, pp. 713–734, 2020.

[36] R. Pecnik and G. Iaccarino, "Predictions of turbulent secondary flows using the $v^2$-$f$ model," in *38th Fluid Dynamics Conference and Exhibit*, p. 3852, 2008.

[37] I. Grigoriev, S. Wallin, G. Brethouwer, and A. Johansson, "A realizable explicit algebraic Reynolds stress model for compressible turbulent flow with significant mean dilatation," *Physics of Fluids*, vol. 25, no. 10, p. 105112, 2013.

[38] S. Girimaji, "Fully explicit and self-consistent algebraic Reynolds stress model," *Theoretical and Computational Fluid Dynamics*, vol. 8, no. 6, pp. 387–402, 1996.